Accurate and robust calibration of the uniform affine transformation between scan-camera coordinates for atom-resolved in-focus 4D-STEM datasets

Accurate and Robust Calibration of the Uniform Affine Transformation Between Scan-Camera Coordinates for Atom-Resolved In-Focus 4D-STEM Datasets

Shoucong Ning[1, 2], Wenhui Xu[3, 4], Yinhang Ma[5], Leyi Loh[1], Timothy J. Pennycook[6], Wu Zhou[5], Fucai Zhang[3], Michel Bosman[1], Stephen J. Pennycook[5], Qian He[1]*, N. Duane Loh[2,7,8]*

1. Department of Materials Science and Engineering, National University of Singapore, 117575, Singapore
2. Center for Bio-Imaging Sciences, National University of Singapore, 117557, Singapore.
3. Department of Electrical and Electronic Engineering, Southern University of Science and Technology, Shenzhen 518055, China
4. Harbin Institute of Technology, Harbin, 150001, China
5. School of Physical Sciences and CAS Key Laboratory of Vacuum Physics, University of Chinese Academy of Sciences, Beijing, 100049, China
6. EMAT, University of Antwerp, Campus Groenenborger, 2020 Antwerp, Belgium
7. Department of Physics, National University of Singapore, 117551, Singapore.
8. Department of Biological Sciences, National University of Singapore, 117557, Singapore.

Abstract: Accurate geometrical calibration between the scan coordinates and the camera coordinates is critical in four-dimensional scanning transmission electron microscopy (4D-STEM) for both quantitative imaging and ptychographic reconstructions. For atomic-resolved, in-focus 4D-STEM datasets, we propose a *hybrid method* incorporating two sub-routines, namely a *J-matrix* method and a *Fourier* method, which can calibrate the uniform affine transformation between the scan-camera coordinates using raw data, without a priori knowledge about the crystal structure of the specimen. The *hybrid method* is found robust against scan distortions and residual probe aberrations. It is also effective even when defects are present in the specimen, or the specimen becomes relatively thick. We will demonstrate that a successful geometrical calibration with *the hybrid method* will lead to a more reliable recovery of both the specimen and the electron probe in a ptychographic reconstruction. We will also show that, although the elimination of local scan position errors still requires an iterative approach, the rate of convergence can be improved, and the residual errors can be further reduced if the *hybrid method* can be firstly applied for initial calibration. The code is made available as a simple-to-use tool to correct affine transformations of the scan-camera coordinates in 4D-STEM experiments.

1. Introduction:

Aberration-corrected scanning transmission electron microscopy (STEM) (Pennycook, 2017) has been indispensable for understanding structural and chemical information of materials at the atomic scale. Recent developments of pixelated single-electron detectors have enabled full diffraction patterns to be recorded at each scanning position with high fidelity and high speeds (Ballabriga *et al.*, 2011; Plackett *et al.*, 2013; Yang *et al.*, 2015; Jiang *et al.*, 2018; Tinti *et al.,* 2018; Ciston *et al.*, 2019; Ercius *et al.*, 2020;). Most recently dwell times have been pushed from the hundreds of microseconds to the 10s of microseconds (O'Leary *et al.*, 2020; Nord *et al.,* 2020) and even to the sub microsecond level (Jannis *et al.*, 2021). This so-called four-dimensional STEM (4D-STEM)(Ophus, 2019; Ophus *et al.*, 2014; Yang *et al.*, 2015) technique has significantly extended STEM's capability by allowing more information to be extracted from the specimen. For instance, 4D-STEM can reveal local electromagnetic fields and directly correlate the functionality of materials with their atomic structures(Gao *et al.*, 2019). Another example is that the development of electron ptychography opens opportunities for obtaining high-spatial-resolution information within a larger field of view than previously possible(Chen *et al.*, 2020). Furthermore, 4D-STEM can be more dose-efficient than conventional STEM methods, and therefore can be used to study beam-sensitive targets (*e.g.*, biological samples) (Pennycook *et al.,* 2015; Yang *et al.*, 2015; Yang *et al.*, 2016; Peltz *et al.*, 2018; Pennycook *et al.,* 2019; Zhou et al., 2020). Among various 4D-STEM techniques, atom-resolved in-focus 4D-STEM (Müller-Caspary *et al.*, 2019; Nguyen *et al.*, 2016; Heimes *et al.*, 2020) has been particularly popular, since having a Z-contrast STEM signal simultaneously available usually helps to effectively extract information from the 4D-STEM dataset (Yang *et al.*, 2016; Wen *et al.*, 2019). Successful implementation of a 4D-STEM experiment requires establishing an accurate geometrical relationship (*e.g.*, scaling, rotation, shearing) between the scanning positions on the sample plane and the diffraction patterns collected on the camera. Such calibration of the scan-camera coordinates is, however, not a trivial task since (i) 4D-STEM is more sensitive to the vortical nature of electron trajectories caused by the electromagnetic lenses compared to other STEM imaging modes that use detectors with circular symmetries; (ii) Most 4D-STEM experiments still need relatively long dwell time (*e.g.*, > 100μs per pixel) making them highly susceptible to instrumental instabilities and environmental disturbances.

We argue that existing calibration methods are not satisfactory to address these challenges. For instance, a pre-experimental calibration, even if it is done perfectly, cannot address the possible variations between different data acquisition sessions due to instrumental instabilities and environmental disturbances. Many post-experimental methods do exist, and they may be classified into two types. On the one hand, the Type I methods directly utilize the ADF-STEM signal or the computed electric field. For instance, imaging registration methods (*e.g.*, Berkels *et al.*(Berkels & Liebscher, 2019; Berkels *et al.*, 2014) and Jones *et*

al.(Jones & Nellist, 2013; Jones *et al.*, 2017)) have recently been applied to 4D-STEM experiments (O'Leary *et al.*, 2021; Jannis *et al.*, 2021). One drawback of this method is the need for multiple ADF-STEM frames from sequential 4D-STEM data, the acquisition of which is still practically challenging for most cameras. This method also did not consider the possible rotations between the scan-camera coordinates. Another popular method was developed based on electric fields by J. Hatchel *et al.* (Hachtel *et al.*, 2018), which was also implemented in the py4DSTEM package by B. Savitzky *et al.* (Savitzky *et al.*, 2021). However, this method did not address possible shearing and scaling of the scanning positions (Jones, 2014; Ning *et al.*, 2018). On the other hand, the Type II methods involve processing the 4D-STEM dataset in Fourier space. For instance, the calibration can be achieved during the iterative ptychography reconstruction via the serial cross-correlation method (Zhang *et al.*, 2013), annealing algorithm(Maiden *et al.*, 2012), nonlinear optimization(Guizar-Sicairos & Fienup, 2008), evolutionary refinement(Shenfield & Rodenburg, 2011), or direct gradient of intensity patterns(Dwivedi *et al.*, 2018). Xu *et al.* (Xu *et al.*, 2020) recently proposed a method that is capable of reconstructing both the scan positions and objects without a priori knowledge of the initial scanning positions. Unfortunately, these methods may not work if the initial scan-position error is large. Their robustness against factors such as residual aberrations is also not well understood.

To overcome the problems mentioned above and establish a more robust and reliable method that can hopefully be universally applied to atom-resolved in-focus 4D-STEM datasets, we hereby introduce a *hybrid method* combining Type I and Type II approaches. In this method, the atom-resolved in-focus 4D-STEM data will be firstly processed via a so-called *J-matrix method*, which calibrates the uniform rotation using the local electric field information. This method is inspired by the method developed by J. Hachtel *et al.* (Hachtel *et al.*, 2018), and it is so named as the Jacobian matrices of electric fields are used. Next, a so-called *Fourier method* will be applied to fully calibrate the affine transformation between the scan-camera coordinates. We will show that this new post-experimental method can effectively calibrate the 4D-STEM dataset without a priori knowledge of the crystal structure of the specimen. The synergistic benefits of using the *hybrid method* will be discussed. For instance, the information obtained from the *J-matrix method* can help eliminate *the Fourier method's* ambiguity. Compared to existing methods, we will show that the *hybrid method* is more robust against initial calibration errors and residual probe aberrations, and it is still effective even when defects are present, or when the specimen becomes relatively thick. With experimental and simulated datasets, we will also show that a successful geometrical calibration will lead to a more reliable recovery of information of both the specimen and the electron probe. Although the refinement of local scan distortions still requires an iterative approach, their rate of convergence can be improved, and the residual errors can be reduced if this *hybrid method* can be firstly applied for initial calibration.

The paper is organized as follows: Firstly, the basic theory of the *J-matrix method* and the *Fourier method* will be introduced and their limitations, when used alone, will be discussed. The workflow of the *hybrid method* will then be discussed. The effectiveness of the *hybrid metho*d will be demonstrated using both simulated and experimental atom-resolved in-focus 4D datasets.

2. Methods

2.1 The J-matrix method.

The scan-camera coordinates used in 4D-STEM data analysis are introduced in **Figure 1**(**a**). On the sample plane, the unit vectors for the fast-scanning direction (***h***) and the slow scanning direction (***v***) of the electron probe form the scan coordinates. Similarly, the camera coordinates, usually Cartesian, are defined on the camera plane in the far-field consisting of unit vectors in the horizontal (***x***) and vertical direction (***y***). The uniform scanning intervals (scaling, Δ) and the uniform rotations (θ) of scanning positions relative to the camera can also be defined. It has been previously shown that, under the weak-phase object approximation (WPOA), the local electric field can be approximated from the integrated Center of Mass (iCoM) of the diffraction patterns (Haas *et al.*, 2020; Lazić *et al.*, 2016; Müller *et al.*, 2014). This approximation was previously tested for samples with thickness up to tens of nanometers(Gao *et al.*, 2019; Addiego *et al.*, 2020). The *J-matrix method* is able to identify the uniform rotation using the computed electric field, which will be altered by the rotations and scaling between the scan-camera coordinates. We can define a Jacobian matrix (J_{scan}) for each scanning position as follows:

$$J_{scan} = \begin{bmatrix} \frac{\partial E_x}{\partial h} & \frac{\partial E_y}{\partial h} \\ \frac{\partial E_x}{\partial v} & \frac{\partial E_y}{\partial v} \end{bmatrix} = \begin{bmatrix} J_1 & J_2 \\ J_3 & J_4 \end{bmatrix} \quad \boldsymbol{EQ1}$$

where E_x and E_y are the horizontal (**x**) and vertical (**y**) components of the electric field obtained from the iCoM in the camera coordinate. For a given atom-resolved in-focus 4D-STEM dataset, the gradient terms in J_{scan} are numerically computed by using the electric field from adjacent scanning positions. After the coordinate transformation (**Supporting Materials S1**), the Jacobian matrix of the electric field in the camera coordinates J_{det} can be expressed as:

$$J_{det} = \begin{bmatrix} \frac{\partial E_x}{\partial x} & \frac{\partial E_y}{\partial x} \\ \frac{\partial E_x}{\partial y} & \frac{\partial E_y}{\partial y} \end{bmatrix} = \Delta \begin{bmatrix} cos\theta & -sin\theta \\ sin\theta & cos\theta \end{bmatrix} J_{scan} \quad \boldsymbol{EQ2}$$

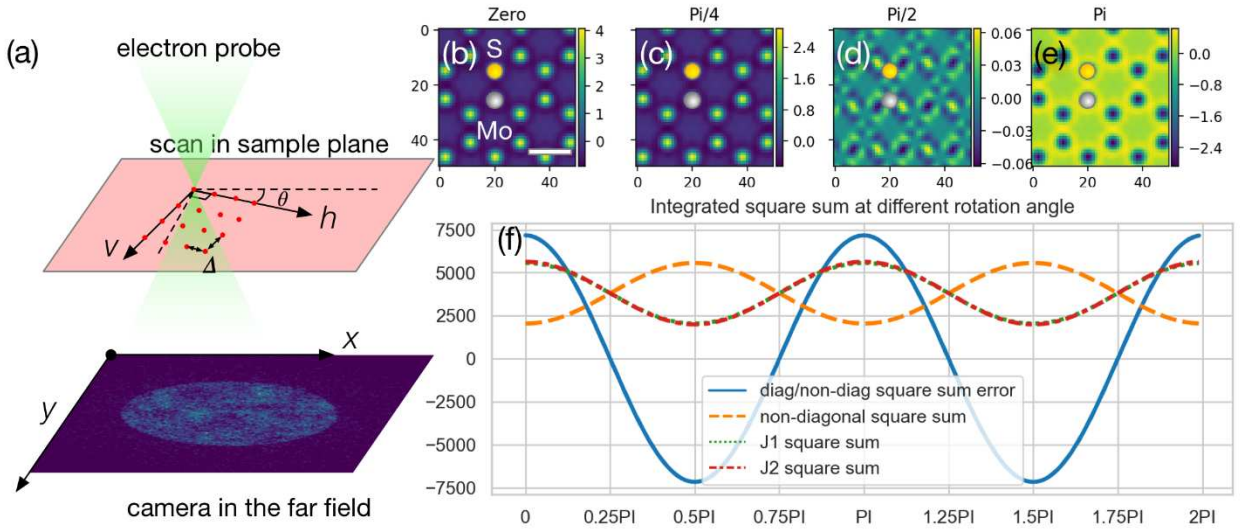

Figure 1. (**a**) The scan-camera coordinates involved in 4D-STEM experiments include the scan coordinates (***h***, ***v***), and the camera coordinates (***x***, ***y***). The (***x***, ***y***) is chosen as the columns and rows of the pixelated camera in the far-field. The raster scan positions on the sample are marked with red dots and the fast-scan and slow-scan directions are labeled as ***h*** and ***v***, respectively. The scan positions on the sample uniquely correspond to each convergent beam diffraction pattern of the 4D-STEM dataset ***I (h, v, x, y)***. The uniform scanning interval is defined as Δ. The uniform rotation angle of (***h***, ***v***) with respect to (***x***, ***y***) is defined as θ. (**b-e**) The computed charge density from a simulated 4D-STEM dataset of a single-layered MoS_2 with different uniform rotation angles (θ equals to 0, π/4, π/2, and π). (**f**) The value of different target functions derived from J_{scan} as a function of the uniform rotation angle θ. The scale bar in *(b)* represents 3.0 Å. The color bars in *(b-e)* represent the dimensionless values from the charge density calculation using the iCoM method. The accelerating voltage used in the simulation was 80kV and more details can be found in **Supporting Materials S2.**

As shown in **EQ2**, when there is no rotation between the scan-camera coordinates and $\theta = 0$, J_{det} is just a scaled version of J_{scan}. Experimentally this will result in the computed charge densities reaching a maximum, as demonstrated in Mo/S sites in a simulated dataset shown in **Figure 1(b).** As the rotation angle θ increases from 0 to π (**Figure 1**(**b-e**)), this computed charge density around the nuclei decreases and eventually appears inverted. This allows us to identify the rotation angle θ by maximizing a certain target function about J_{det}. In this *J-matrix method*, the difference between the spatial integration of squared diagonal and non-diagonal terms of J_{det}, as a function of θ, can be used as the target function, and similar target functions were used in previous works by J. Hachtel *et al.* and B. Savitzky *et al.* (Hachtel *et al.*, 2018; Savitzky *et al.*, 2021). The gradient of the target function reaches zero when:

$$tan2\theta = 2\sum(J_2J_4 - J_1J_3) / \sum(J_1^2 + J_4^2 - J_2^2 - J_3^2)$$ ***EQ3***

where J_1, J_2, J_3, J_4 are defined in **EQ1**. The detailed derivation of **EQ3** can be found in the **Supporting Materials S3**. This target function is found to be very sensitive to the uniform rotation angle θ, as shown in **Figure 1(f)**. However, solving the θ analytically from **EQ3** will result in four possible solutions in the range [0, 2π]. Two of the solutions can be excluded as the corresponding integration of squared diagonal terms of J_{det} are negative. From the remaining two possible solutions of θ that are 180° apart, one unique solution can be obtained by introducing an ADF-weighted *J-matrix* J_W:

$$J_W = WJ_{det}$$ ***EQ4***

where W represents the corresponding ADF intensity at each pixel in practice. Interestingly, if there is a chirality change between the scan coordinates (***h, v***) and the camera coordinates (***x, y***), it can be directly observed from the sign of diagonal terms of J_W. The detection and compensation of such a chirality change is critical for ptychographic reconstructions as demonstrated in **Supporting Materials S4**. More details about the ADF-weighted *J-matrix* can be found in the **Supporting Materials S5**.

Figure 2 and **Table 1** show an application example of the *J-matrix method* using numerical simulations of a MoS_2 monolayer sample where the ground truth of the uniform rotation angle is known. While the *J-matrix method* is effective in roughly determining the uniform rotation angle correctly, it is also obvious that various factors, including residual aberrations, the scanning step size, the magnitude of any uniform rotation, and even the rotation angle error itself can significantly impact the calibration accuracy. The reason for these increased errors could be for instance attributed to the reduced continuity of the electric field and hence less meaningful use of the J-matrices. Additional discussions about the influence of other factors such as scanning step size, camera tilt, camera gain distribution, camera point spread function, and sample thickness can be found in **Supporting Materials S6**. Clearly, the *J-matrix method*, when used alone, is not an accurate solution for the geometric calibration of 4D-STEM datasets.

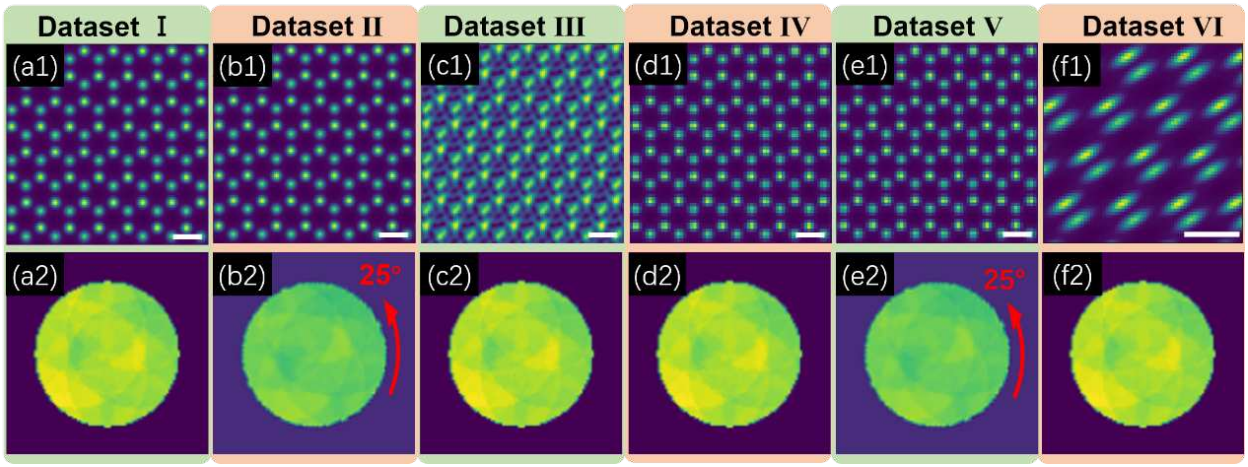

Figure 2. Simulated in-focus 4D-STEM datasets of monolayer MoS_2 with different imaging parameters (see **Table 1**). ADF images obtained from the 4D-STEM dataset in (**a-f**) are chosen to represent these datasets. (**a-b**) The scanning step size is set to 0.17 Å along both horizontal and vertical directions, and this dataset is simulated with perfect conditions. One typical CBED pattern of the 4D-STEM dataset is shown in (**a2**), and the CBED patterns are rotated by 25° in (**b2**). (**c**) Probe-forming lens aberration is introduced by setting first- and second-order astigmatisms with zero azimuthal angles to 5nm and 40 nm, respectively. The coma is set to 30 nm and the azimuthal angle is set to zero. (**d-e**) The scanning step size is increased to 0.34 Å. The other settings are kept the same as (**a**) and (**b**), respectively. In (**f**), the rotation angle of the slow scanning direction is set to be 22.5°, and the step sizes of the fast and slow scanning direction are set to 0.34 and 0.48 Å, respectively. The number of scanning positions is reduced from 256*256 to 64*64. Scale bars in (**a1**-**f1**) represent 3.0 Å. The accelerating voltage used in the simulation was 80kV and more details can be found in **Supporting Materials S2**

Table 1. Key microscope parameters in the simulation of 4D-STEM in **Figure 2**.

Datasets in Figure 2	**I**	**II**	**III**	**IV**	**V**	**VI**
With aberration	N	N	Y	N	N	N
Scan step size (Å)	0.17	0.17	0.17	0.34	0.34	0.17
True rotation angle	0°	25°	0°	0°	25°	22.5°
Calibrated rotation angle θ using the *J-matrix method*	0.02°	26.02°	0.72°	0.03°	30.41°	32.16°
Calibration error	0.02°	1.02°	0.72°	0.03°	5.41°	9.66°

2.2 The Fourier method.

Figure 3 demonstrates a Type II calibration method which we call the *Fourier method*. A 4D-STEM dataset ***I(h, v, x, y)*** is visualized in **Figure 3(a)**, where each sample pixel corresponds to a diffraction pattern displayed in the camera coordinates (***x, y***), and the diffraction patterns are organized according to probe positions (***h, v***). A 2D Fourier transform with respect to probe scanning positions (***h, v***) was applied which converted ***I(h, v, x, y)*** into the so-called G-sets (Rodenburg & Maiden, 2019) — ***G(k_h, k_v, x, y)***, where (***k_h, k_v***) are the corresponding reciprocal vectors of the (***h, v***). **Figure 3(b)** visualizes the slices of the ***G(k_h, k_v, x, y)*** at specific scanning spatial frequencies tiled in the (***k_h, k_v***) coordinates. Under the weak phase object approximation (Pennycook *et al.*, 2015), a slice in the G-sets (**Figure 3(c)**) can be approximated to contain a central disk and two first-order disks. The amount and the direction of these first-order disks displaced relative to the central disk reveal information of the scanning intervals and rotation angles and are functions of the scanning spatial frequencies (*i.e.*, the index (*i, j*) in the (***k_h, k_v***) coordinates). Consequently, the geometric parameters needed for the calibration can be determined by investigating these slices at known scanning spatial frequencies.

Assuming there is an affine transformation between the scan-camera coordinates, the fast (***h***) and slow (***v***) scanning directions then no longer share a uniform rotation angle and scanning interval (**Figure 4**(**a**) and (**d**)). We can define the scanning intervals along ***h*** and ***v*** as Δ and $\gamma\Delta$, and the rotation angles of these two directions as θ_x and θ_y, respectively. According to the reciprocal relationship between (***h, v***) and (***k_h, k_v***) coordinates, the shift vector **Q** of the first-order disks in a G-sets slice like **Figure 3(c)** is given as:

$$\boldsymbol{Q} = (i * cos\,\theta_y - j * \gamma sin\,\theta_x\,, i * sin\,\theta_y + j * \gamma cos\,\theta_x\,)/\Delta' \quad \boldsymbol{EQ5}$$

where i and j are the indexes of a G-sets slice in **Figure 3**) relative to the central disk in the ***k_h*** and ***k_v*** directions, respectively. $1/\Delta'$, which is related to Δ, is the reciprocal scanning interval along the ***k_h*** direction. The intersection angle of **Q** with the ***x*** direction is labeled as α **(Figure 3(c))**. The detailed derivation of **EQ5** can be found in the **Supporting Materials S7**. The shift vector **Q** can be directly measured from the slices in the G-sets slices. Then θ_x, θ_y, Δ' and γ in **EQ5** can in principle be determined by solving an equation group using **Q** values derived from at least two slices in the G-sets.

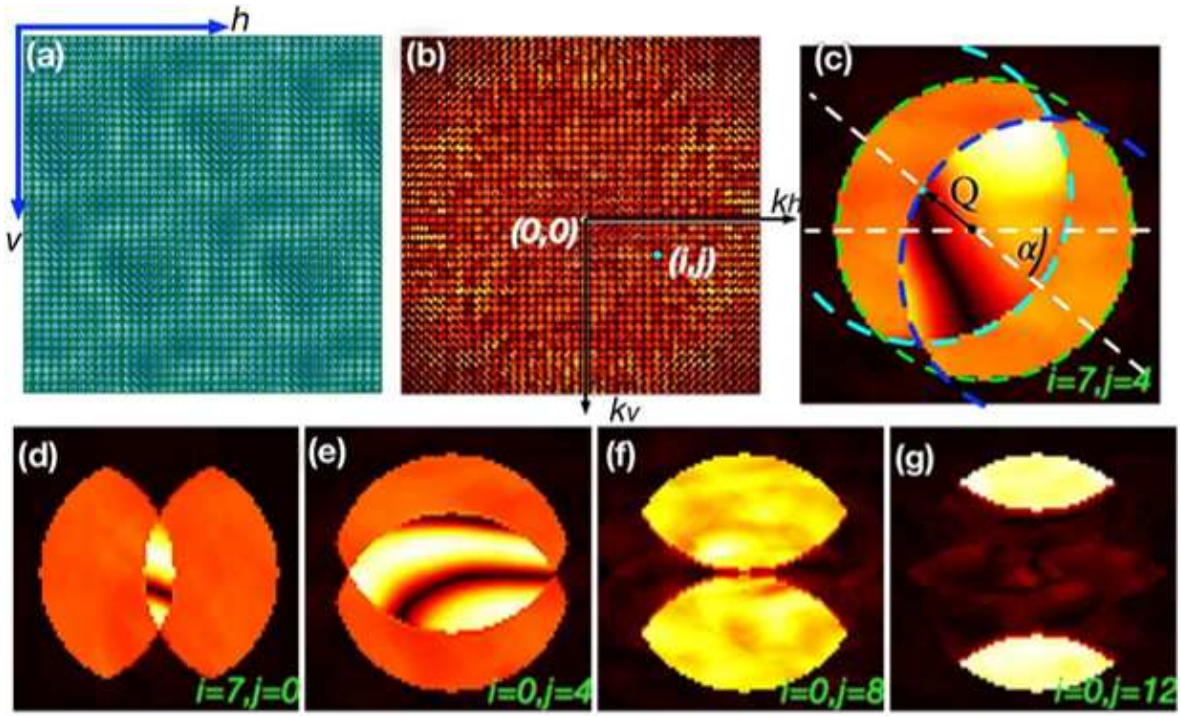

Figure 3. The illustration of the *Fourier method* for the calibration of the affine transformation between the scan-camera coordinates. **(a)** A visualization of a simulated 4D-STEM dataset ***I(h, v, x, y)*** of a single layer MoS_2, with each pixel being a diffraction pattern in the camera coordinates (**x, y**), and the diffraction patterns are organized according to probe positions (***h, v***). **(b)** A visualization of the G-sets ***G(k_h, k_v, x, y)*** after the 4D-STEM dataset ***I(h, v, x, y)*** being Fourier transformed with respect to the probe positions (***h, v***). **(c)** A slice in the G-sets with the indexes of $i = 7$ and $j = 4$ with respect to the central disk on the (***k_h, k_v***) coordinates, which represent the spatial frequencies of the probe positions. The central disk and the first-order disks have been outlined, and the shift vector **Q** and its angle α are highlighted. (**d-g**) Additional slices of the G-sets at different positions on the (***k_h, k_v***) coordinates. The accelerating voltage used in the simulation was 80kV and more details can be found in **Supporting Materials S2.**

Unlike the *J-matrix method*, the *Fourier method* can calibrate the affine transformation between the scan-camera coordinates. Such a calibration only relies on locating the central and first-order disks in the G-sets. When the WPOA is applied, this can be performed by fitting the positions of the shifted disks. Consequently, the factors such as the lens aberrations and the scanning step size do not affect the calibration results significantly, unlike the case for the *J-matrix method*. The accuracy of the rotation angle and scanning interval is determined by the precision of positioning the first-order disks and the shift vector **Q**. Hence, high spatial frequency G-sets slices (*i.e.*, larger indices of i and j) are usually preferred to achieve higher accuracy, since the first order disks in those slices are better separated and smaller relative measurement errors can be achieved. Notice that the *Fourier method* so far only utilizes the WPOA and does not require

the sample to be crystalline. Also, notice that the *Fourier method* here did not consider localized small deviations in scanning positions. In the **Supporting Materials S8**, the technical details of the **Q** fitting algorithms and detailed workflow of the *Fourier method* are provided.

However, one main drawback of the *Fourier method* is that one cannot obtain an unique set of solutions for the rotation angles since if the set (θ_x, θ_y) satisfies **EQ5** under the constrain of positive γ, so does the set of $(\theta_x + 180°\,, \theta_y + 180°)$. Misaligning the Scan-Camera coordinates by 180 could result in mistakes correlating the 4D-STEM results with other data such as electric field mapping for instance. As we will show in the next section, the result obtained from the *J-matrix method*, although being less accurate, can help to eliminate this ambiguity, which is one of the major synergistic benefits of *the hybrid method*.

2.3 The hybrid method

A typical workflow of the *hybrid method* is schematically shown in **Figure 4.** First the dataset is processed using the *J-matrix method* so that the uniform rotation angle can be obtained and possible flips between the scan-camera coordinates can be detected. Then the *Fourier method* is applied to fully calibrate the affine transformation, where the information acquired from the *J-matrix method* earlier can help to identify the unique solutions during the calibration of affine transformations. In addition, the geometric parameters determined by the *J-matrix method* provide credible initial positions of the first order disks in the G-sets slices that will help to achieve a more accurate determination of the **Q** vectors needed in the *Fourier method*.

In the following sections, we will use simulated and experimental datasets to demonstrate the effectiveness of this *hybrid method*, where better calibration leads to more reliable ptychography reconstruction and post-experimental aberration correction. We will also show that the *hybrid method* works well for thin samples and for relatively thick samples up to a few tens of nanometers.

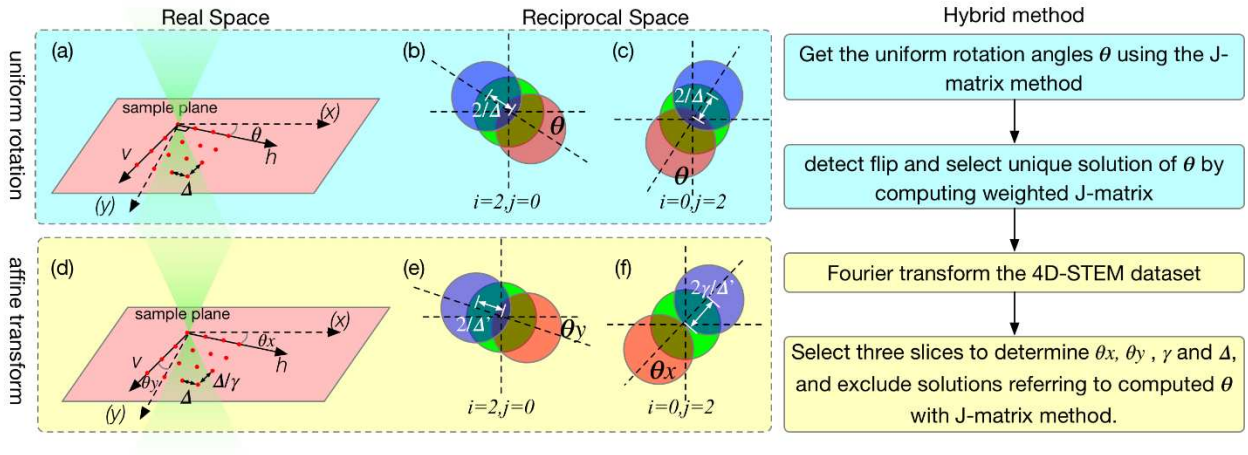

Figure 4. A comparison between the uniform rotation and the affine transformation of scanning positions. In the real space, the scanning positions are rotated relative to the camera with the same angle as shown in (**a**). In the reciprocal space, two first-order disks are shifted relative to the bright field disk in (**b**) and (**c**). The intersection angle between the horizontal direction and the shift direction in (**b**) is the rotation angle of the scanning positions. Similarly, the measured angle between the shift direction and the vertical direction is also θ in (**c**). Considering the affine transformation, the rotation angle of the fast and slow scanning directions are defined as θ_x, θ_y in (**d**), respectively. In addition, the scanning step size along the slow scanning direction is changed to Δ/γ. (**e, f**) In reciprocal space, the intersection angle between the shift direction and the vertical and horizontal direction becomes θ_x and θ_y, respectively. Moreover, the scanning intervals also affect the displacement of the bright field disk as shown in (**f**).

3. Application Examples and Discussions

To demonstrate the effectiveness of the *hybrid method*, we firstly examine a simulated dataset for which the ground truth is known. The simulated dataset **VI** of the single-layer MoS_2 previously shown in **Figure 2** and **Table 1** was used for this purpose and the calibration results are shown in **Figure 5**. If the dataset is only calibrated with the *J-matrix method*, the uniform rotation angle is found to have relatively large errors, which is illustrated as obvious mismatches between the disks in the G-sets slices and the cyan outlines drawn using the calibrated geometric parameters (**Figure 5(a-c)**). This has caused apparent errors in the ptychographic reconstruction using the single-sideband (SSB) method (Pennycook *et al.*, 2015) shown in **Figure 5(d)**, where the MoS_2 structure has not been accurately recovered. In sharp contrast, when the *hybrid method* was applied, the disk locations could be identified much more accurately, and the reconstruction recovered the single-layer MoS_2 structure nicely (**Figure 5(e-h)**). Moreover, having an accurate geometric calibration is critical for post-experiment probe aberration correction. The error in the recovered phase of the probe compared to the ground truth (**Figure 5(i)**, **Table 2**) gets increasingly more apparent when the

rotation angle error changes from 0°, 2.5°, and 5°, as shown in **Figure 5(j - l)**, respectively. More details about the residual aberration correction using the *Fourier method* are given in **Supporting Materials S9**.

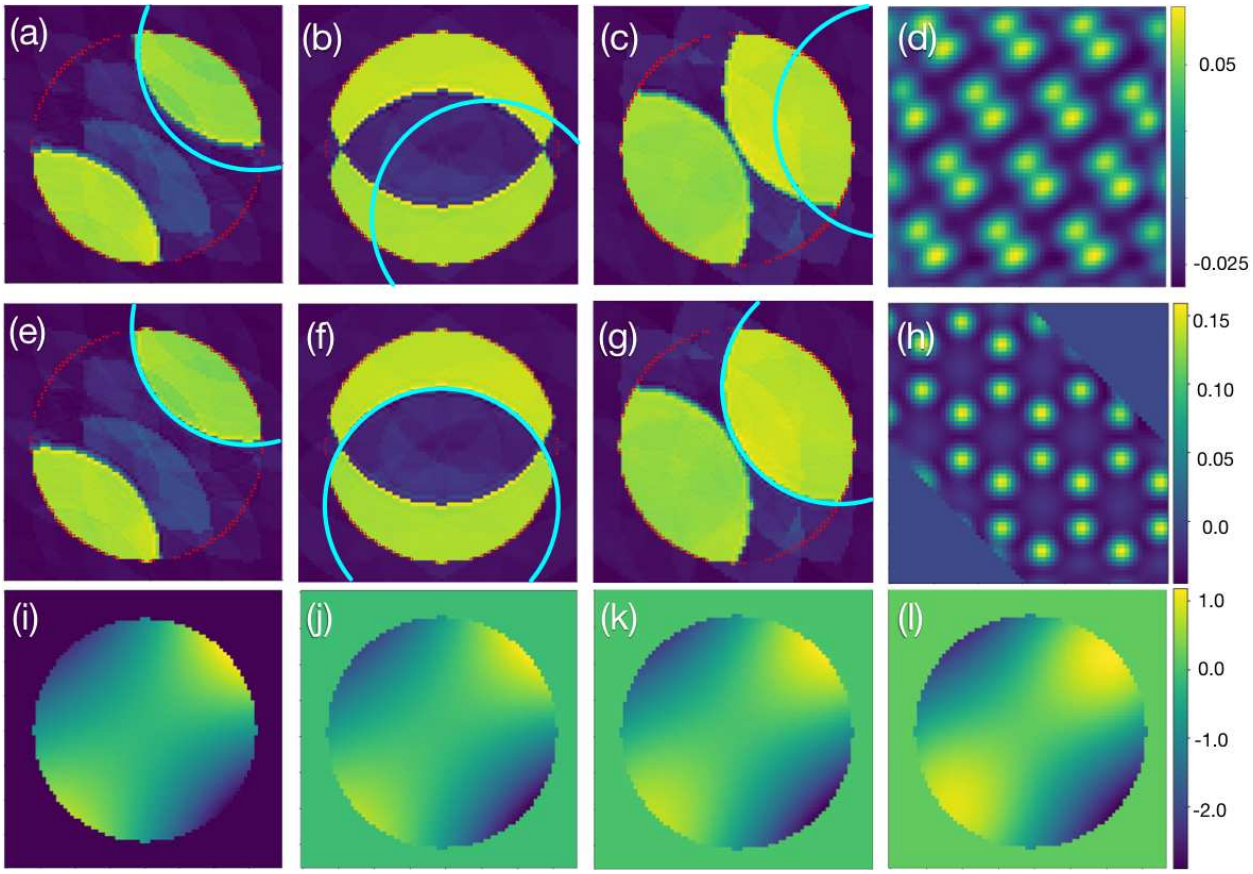

Figure 5. Illustration of benefits of the *hybrid method* using the simulated dataset **VI** shown in **Figure 2** and **Table 1**. (**a**-**c**) Determined shifted disk positions (cyan curves) using the uniform rotation angle determined by the *J-matrix method*. (**d**) The reconstructed phase angle of monolayer MoS_2 with the SSB method according to geometric parameters determined by the *J-matrix method*. (**e-g**). Determined shifted disk positions using the uniform rotation angles obtained using the *hybrid method*. (**h**) The reconstructed phase of monolayer MoS_2 with the SSB method according to geometric parameters determined by the *hybrid method*, the affine transformation is applied to (**h**). (**i**) The phase shift in the aperture of the probe forming lens according to the aberration coefficient listed in **Table 2**. (**j-l**) The phase map determined using the SSB method in the aperture of the probe forming lens when the rotation angle error is 0°, 2.5°, and 5°, respectively. A good match between the (**i**) and (**j**) is observed, and the discrepancy becomes more obvious with the increasing rotation angle error in the cases of (**k**) and (**l**). Color bars represent the phase shift in radians.

Table 2. Aberration coefficient in the probe forming lens in **Figure 5 (i)**. A1, A2 and B2 represent the 2-fold astigmatism, 3-fold astigmatism and coma, respectively.

Aberration type	**defocus**	**A1**	**A2**	**B2**	**3rd Spherical aberration**
Value	1.0nm	3.0nm	10nm	20nm	0.2um
Angle	-	0	0	0	-

The *hybrid method* was also tested using experimental data. **Figure 6 (a)** is an ADF image computed from an experimental in-focus 4D-STEM dataset of monolayer MoS_2. The yellow and red arrows indicate the fast and slow scan directions, respectively. Using the *J-matrix method* alone, the uniform rotation angle was determined to be -0.25 rad (14.32°), and a flip of the fast-scanning direction is detected as indicated by the yellow and red arrows in **Figure 6 (c)**. After applying the *hybrid method*, an affine transformation was found with θ_x, θ_y, γ values being 3.00 rad (172.89°), -0.26 rad (14.90°), and 1.17, respectively. The effectiveness of the *hybrid method* was evidenced by a more accurate determination of the first-order disk positions in a G-sets slice, compared to the one drawn using the rotation angle obtained from the *J-matrix method* (**Figure 6 (b)**). It can also be evidenced from the resulting ptychographic reconstruction. The MoS_2 lattice was distorted if only considering the uniform rotation using the *J-matrix method* (**Figure 6 (c)**), while the hexagonal ring of atoms was much better recovered after considering the affine transformation using the *hybrid method* (**Figure 6 (d)**). The structure of the MoS_2 lattice is reliably recovered when using the geometric parameters determined by the *hybrid method* as the same highlighted MoS_2 ring shown in **Figures 6** (**d**). Notice that during the calibration and the reconstruction processes, no a priori information about the structure of the MoS_2 was used. **Supporting Materials S10** shows the iteratively reconstructed results via ePIE (Maiden & Rodenburg, 2009) using the same datasets as above. Comparing the power spectra (Figure S7), the symmetry of the MoS_2 lattice was better recovered in the case where the data has been pre-calibrated using *the hybrid method*, compared to the counterpart pre-calibrated with *the J-matrix method*. Clearly, the iterative method cannot simply replace the calibration of the uniform affine transformation. More on the benefits of pre-calibrating the 4D-STEM dataset before applying iterative reconstruction will be discussed later. **Supporting Materials S11** shows additional 4D-STEM datasets and their calibration results of the same sample obtained subsequently to the one shown in **Figure 6**. The calibration results are slightly different on each acquisition, which re-emphasize the importance of the post-experimental calibration as the geometrical parameters are changing even if the data were taken using the same instrument consecutively.

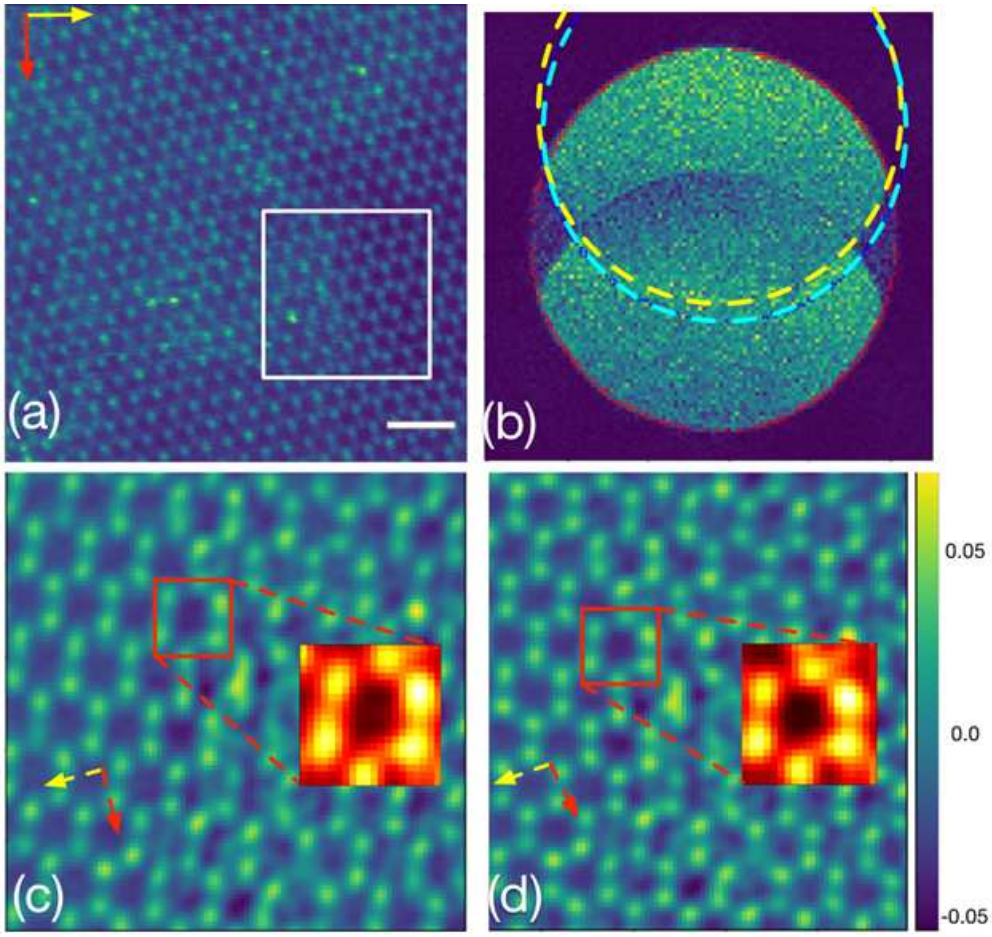

Figure 6. (**a**) The ADF-STEM image corresponds to an experimental 4D-STEM dataset of monolayer MoS_2 acquired using a JEOL ARM200CF operating at 80 kV. (**b**) The difference between the first-order disk positions in a G-sets slice using geometrical parameters that were determined by the *J-matrix method* (cyan ring) and by the *hybrid method* (yellow ring). Reconstructed phase distribution from the area highlighted by the white rectangle in (**a**) using the SSB methods with the geometrical parameters determined by **(c)** the *J-matrix method* and **(d)** by the *hybrid method*. A change in the chirality was detected in both cases, as marked by the red arrows in (**a**), (**c**), and (**d**). The residual aberrations in the electron probe are fitted based on the determined disk positions and corrected in both (**c**) and (**d**). Scale bar in (**a**) represents 1 nm and color bar represents the phase shift in radians.

Interestingly, the *hybrid method* was found to work well in the case of relatively thick specimens. A series of simulated data using AA stacked MoS_2 with sample thickness ranging from 3 Å to 30 nm was summarized in **Supporting Materials S12**. As shown in **Figure S9**, for G-sets slices with lower spatial frequencies (*i.e.*, smaller i, j indices), the outlines of the first-order disks in the G-sets become less recognizable as the sample thickness increases. However, for G-sets slices with higher spatial frequencies

(*i.e.*, larger i, j indices), the outlines can still be visually identified even when the specimen becomes thicker, hence making the calibration with the *hybrid method* feasible. The calibration results of the simulated dataset using a 30 nm AA stacked MoS_2 specimen is shown in **Figure 7** as an example. The distortion of the scanning positions was introduced by rotating the slow scanning direction by -10° (anti-clockwise). The scanning step size along both fast and slow directions is 0.17 Å. The *J-matrix method* was used first and a uniform rotation angle of -5.3° was found. Despite the inaccuracy, the positions of the first-order disks for four G-sets slices at different spatial frequencies estimated using this uniform rotation angle are visually close to the true value, as shown by the cyan rings in **Figure 7**. (**a-d**). The positions of the first-order disks can be further refined by the algorithms given in the **Supporting Materials S8**. The result is shown as yellow dashes in **Figure 7** (**a-d**). Using the *Fourier method*, the geometric parameters θ_x, θ_y and γ were determined to be 0.2°, -9.6° and 0.98 respectively, which are much closer to the ground truth value of 0°, -10° and 1.0, compared to the previous case. The benefit of having a more accurate geometric calibration can be visualized by reconstructing the annular bright field image (ABF) from the 4D-STEM dataset. The hexagonal rings are clearly more distorted in the ABF image calibrated by the *J-matrix method* (**Figure 7(e)**) than the one calibrated by the *hybrid method* (**Figure 7(f)**).

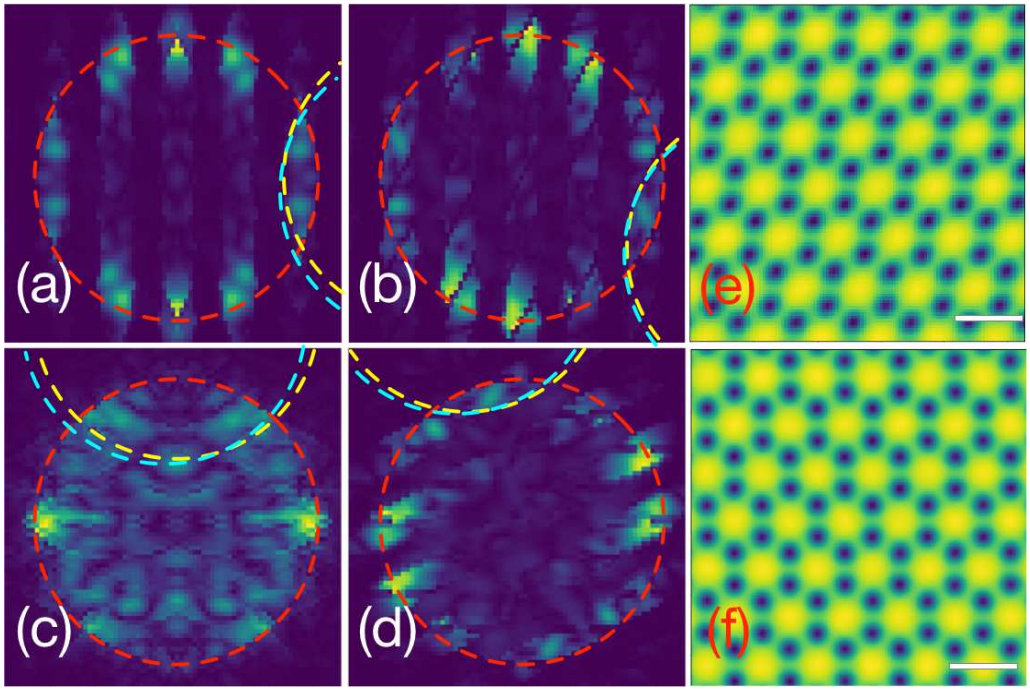

Figure 7. The simulated 4D-STEM dataset of a relatively thick MoS_2 sample with an affine transformation exists between the scanning coordinates and the camera coordinates. The rotation angles of the fast and slow scanning direction are 0° and -10°, respectively. (**a-d**). Slices of the Fourier-transformed 4D-STEM dataset at different probe frequencies. The indices of these frequencies are (23, 4), (23, 11), (0, 19), (6, 24), respectively. The cyan circles are the outline of the shifted disks determined using the *J-matrix method*, and

the yellow curves are located using the *hybrid method*. (**e**) The corresponding ABF-STEM image of the original 4D-STEM dataset, the *J-matrix method* is not able to correct the distortion in this image. (**f**). The affine-transformed ABF-STEM image using the geometric parameters determined using a *hybrid method*. Scale bars in (e) and (f) represent 3 Å. The accelerating voltage used in the simulation was 80kV and more details can be found in **Supporting Materials S2.**

So far, we have shown that the *hybrid method* is highly effective in correcting the possible affine transformation between the scan-camera coordinates. However, experimental 4D-STEM data often also contains localized and non-uniform scan distortions and the correction of which still requires an iterative ptychographic method or multiple frame 4D-STEM (O'Leary *et al.*, 2021; Jannis *et al.*, 2021) where non-rigid registration technologies can also be used. In this section, we find that a more credible initial probe position provided by the initial calibration via the *hybrid method* will benefit iterative methods (*e.g.*, ePIE (Maiden & Rodenburg, 2009)) by accelerating its convergence and reducing the residual errors. A simulated 4D-STEM dataset of monolayer MoS_2 was used as an example, where an affine transformation and additional local scanning distortions were deliberately introduced. The slow scanning direction is rotated by 10° (clockwise). Local scanning distortions are modelled in this simulation by perturbing each scanning position with a random shift following the linear distribution ranging from 0 to 0.3 Å. The acceleration voltage, step size, and aperture size of the probe forming lens are set to 80kV, 0.17 Å and 24 mrad, respectively. The number of scanning position is 64*64, indicating a 1.1*1.1 nm^2 scanned area. This simulated dataset was first calibrated using the *J-matrix method*, and a uniform rotation of 7.2° was found. As a comparison, the same dataset was also calibrated using the *hybrid method*, and θ_x, θ_y and γ were found to be 0.1°, 9.8°, and 1.01 respectively. Then the probe positions were iteratively refined to account for the localized distortions. As shown in **Figure 8 (a)** and **(b)**, the reconstruction with a better initial probe position calibrated by the *hybrid method* reproduces the MoS_2 lattice much better than the counterpart with the *J-matrix method*. The difference made by having more reliable initial probe positions for the iterative methods can be better visualized if the residual errors can be plotted as a function of the iterative numbers (**Figure 8** (**c**) and (**d**)). The error is the difference between the simulated diffraction patterns and the one computed using the object and probe function in each iteration. Clearly, the case with initial probe positions calibrated with the *hybrid method* has led to a faster convergence and smaller residual errors.

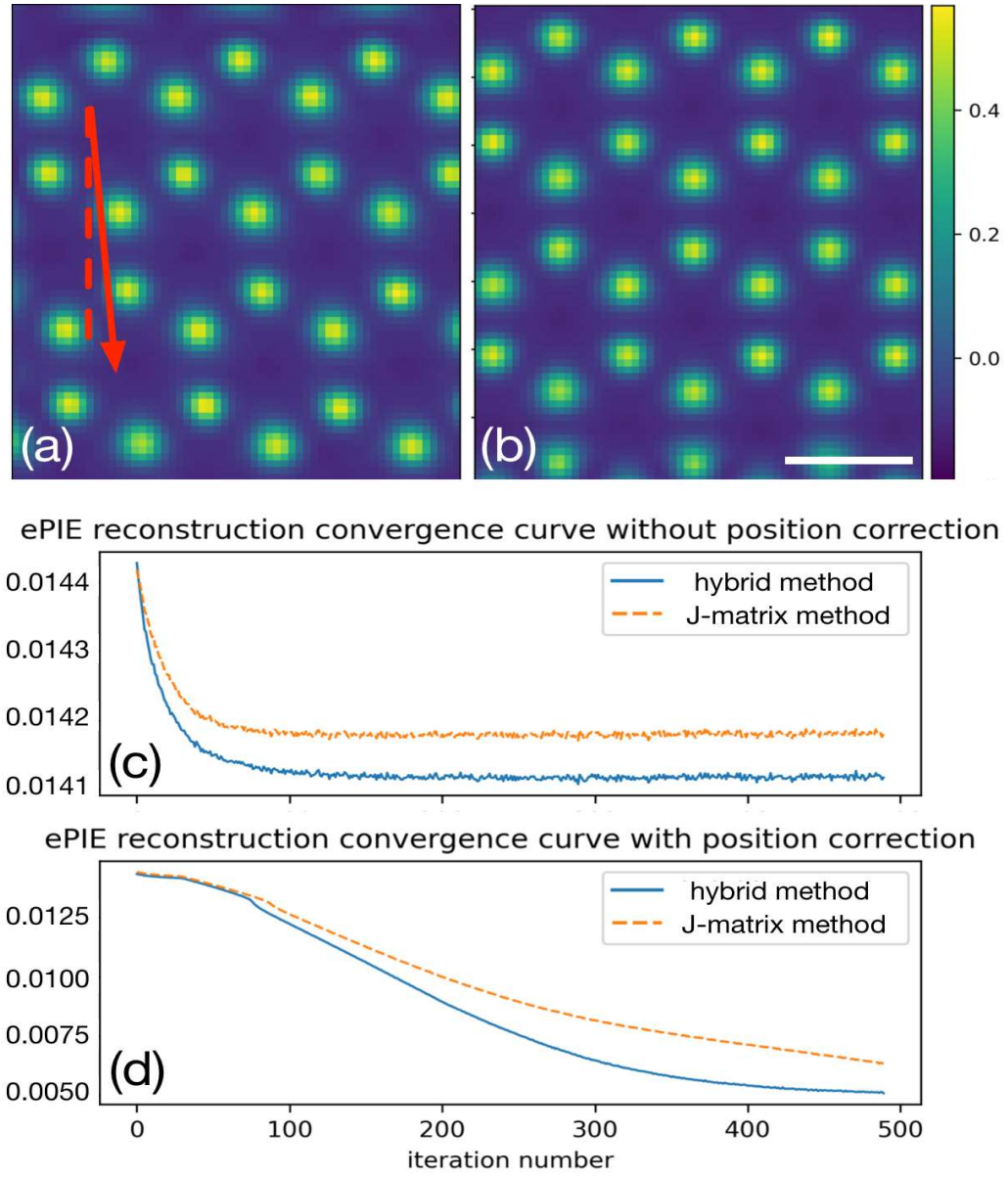

Figure 8. (**a, b**) Reconstructed phase using the geometric parameters determined using *the J-matrix* and *the hybrid methods* from simulated 4D-STEM dataset, respectively. The ePIE method is adopted in the ptychography reconstruction, and the correction of probe positions is applied. (**c**-**d**) The convergence curve of the errors between the estimated diffraction intensities and the recorded CBED patterns versus the iteration numbers. The probe position was fixed in the first 500 iterations as shown in (**c**), and position correction is enabled in the following 500 iterations as shown in (**d**). The scale bar represents 3 Å and the color bar represents the phase shift in radians. The accelerating voltage used in the simulation was 80kV and more details can be found in **Supporting Materials S2.**

Moreover, the effect of lowering the electron dose on *the hybrid method* was investigated using simulated data (**Supporting Materials S13**) with 80kV electrons and 128 by 128 probe positions, where the doses were set to change from 6.6×10^5 e/Å (the dose usually adopted for experimental HAADF imaging) to 6.6×10^4 and then to 6.6×10^3 e/Å. In other words, the averaged number of electrons per diffraction pattern in these cases will be about 20000, 2000, and 200, respectively. As shown in **Figure S10**, both the *J-matrix* and the *hybrid method* remain effective and calibrated rotation angles very close to the true value of 0° (<0.1° difference) in the cases of both 20000 and 2000 electrons per diffraction pattern. In the case of 200 electrons per diffraction pattern, both methods remain effective, but the errors have gone up as the calibrated uniform rotation angles show clear deviations from 0° (*i.e.*, the *J-matrix method* (0.840°) and the *Fourier method* (0.410°). As the dose decreases, the local electric field measurement will become noisier and less continuous, which in turn degrades the accuracy of the *J-matrix method*. On the other hand, for *the Fourier method*, lowering the electron dose will make it more difficult to correctly identify the outline of the disks in the G-set slices. Interestingly, as shown in **Figure S11**, if the total number of electrons was kept the same for the 4D-STEM datasets, but the dose (e/Å) decreases as the probe scanning intervals increases, the accuracy of the *J-matrix method* degrades again, but the accuracy for the *Fourier method* remains largely unchanged. This can be understood as *the Fourier method* assesses the data as a whole so the signal to noise in the G-sets is mostly concerned with the total number of electrons. This finding gives one practical strategy to maintain or increase the necessary calibration accuracy, which is to keep or increase the total number of electrons in the dataset when increasing electron dose (e/Å) is not an option. We will explore more on this in follow-up work.

Last but not least, in order to further illustrate the point that the *hybrid method* does not rely on *a priori* knowledge of the crystallinity of the specimen, a simulated 4D-STEM dataset of amorphous carbon was tested (**Supporting Materials 14**). As shown in **Figure S12**, the *J-matrix* method is effective for determining the overall rotation angle using the target function discussed in **Figure 1**. The *Fourier method* also remains effective, since the disks in the G-set slices are clearly visible, hence the values of the **Q** vectors and angle α defined in **Figure 3** can be obtained. Hence we can safely say that the material is not the limiting factor for the hybrid method to be effective, as long as the weak phase object approximation holds.

4. Conclusion:

To summarize, in this work, we have proposed a *hybrid method* to effectively calibrate possible affine transformations between the probe scanning positions and the 4D-STEM cameras. The *hybrid method* incorporates two complementary sub-routines, namely the *J-matrix method* and the *Fourier method.* The *Fourier method* is found to be more accurate and robust, while the *J-matrix method* helps to find a unique calibration solution within the *Fourier method*. Using simulated and experimental data, we have shown that *the hybrid method* works without *a priori* knowledge about the crystallinity of the specimen and remains effective when there are defects in the specimen or when the sample becomes relatively thick. Although our method only deals with the uniform or isotropic affine transformation of scanning positions relative to the camera, many localized and non-uniform scan distortions do exist in practice. We showed that a successful calibration of the uniform distortion will establish a more credible starting point and leads to a more reliable recovery of both the specimen and the electron probe in iterative reconstruction. The *hybrid method* was also found effective with noisy 4D-STEM data when the electron dose decreases, although the calibration accuracy can indeed be compromised if the data becomes too noisy. We show that one practical way of maintaining the necessary calibration accuracy is to keep or increase the total number of electrons in the dataset when increasing electron dose (e/Å) is not an option. A final remark is that although using the *hybrid method* will be more computationally demanding compared to using the *J-matrix* method alone, for a typical dataset such as the one shown in Figure 8, the code can be run on personal computers and usually finishes within a few minutes (see **Supporting Materials 15**). The benefits of using the hybrid method certainly outweigh the additional computational cost. The improved quality and reproducibility of 4D-STEM data analysis with this method will hopefully accelerate the adoption of the 4D-STEM technique for materials research.

Acknowledgment

N. D. Loh kindly acknowledges support from NUS Early Career Research Award (R-154-000-B35-133), MOE's AcRF Tier 1 grant nr. R-284-000-172-114 and NRF CRP grant number NRF-CRP16-2015-05. Q. He would also like to acknowledge the support of the National Research Foundation (NRF) Singapore, under its NRF Fellowship (NRF-NRFF11-2019-0002). W. Zhou acknowledges the support from Beijing Outstanding Young Scientist Program (BJJWZYJH01201914430039). F. Zhang acknowledges the support of the National Natural Science Foundation of China (11775105, 12074167). T. J. Pennycook acknowledges funding under the European Union's Horizon 2020 research and innovation programme from the European Research Council (ERC) Grant agreement No. 802123-HDEM.

The source code is available at https://github.com/ningustc/4DSTEM-Calibration.

Reference

Addiego, C., Gao, W. & Pan, X. (2020). Thickness and defocus dependence of inter-atomic electric fields measured by scanning diffraction. *Ultramicroscopy* **208**, 112850.

Ballabriga, R., Campbell, M., Heijne, E., Llopart, X., Tlustos, L. & Wong, W. (2011). Medipix3: A 64k pixel detector readout chip working in single photon counting mode with improved spectrometric performance. *Nuclear instruments & methods in physics research. Section A, Accelerators, spectrometers, detectors and associated equipment* **633**, S15–S18.

Berkels, B., Binev, P., Blom, D. A., Dahmen, W., Sharpley, R. C. & Vogt, T. (2014). Optimized imaging using non-rigid registration. *Ultramicroscopy* **138**, 46–56.

Berkels, B. & Liebscher, C. H. (2019). Joint non-rigid image registration and reconstruction for quantitative atomic resolution scanning transmission electron microscopy. *Ultramicroscopy* **198**, 49–57.

Chen, Z., Odstrcil, M., Jiang, Y., Han, Y., Chiu, M.-H., Li, L.-J. & Muller, D. A. (2020). Mixed-state electron ptychography enables sub-angstrom resolution imaging with picometer precision at low dose. *Nature communications* **11**, 2994.

Ciston, J., Johnson, I. J., Draney, B. R., Ercius, P., Fong, E., Goldschmidt, A., Joseph, J. M., Lee, J. R., Mueller, A., Ophus, C., Selvarajan, A., Skinner, D. E., Stezelberger, T., Tindall, C. S., Minor, A. M. & Denes, P. (2019). The 4D Camera: Very High Speed Electron Counting for 4D-STEM. *Microscopy and Microanalysis* **25**, 1930–1931.

Dwivedi, P., Konijnenberg, A. P., Pereira, S. F. & Urbach, H. P. (2018). Lateral position correction in ptychography using the gradient of intensity patterns. *Ultramicroscopy* **192**, 29–36.

Gao, W., Addiego, C., Wang, H., Yan, X., Hou, Y., Ji, D., Heikes, C., Zhang, Y., Li, L., Huyan, H., Blum, T., Aoki, T., Nie, Y., Schlom, D. G., Wu, R. & Pan, X. (2019). Real-space charge-density imaging with sub-ångström resolution by four-dimensional electron microscopy. *Nature* **575**, 480–484.

Ercius, P., Johnson, I., Brown, H., Pelz, P., Hsu, S.-L., Draney, B., Fong, E., Goldschmidt, A., Joseph, J., Lee, J., Ciston, J., Ophus, C., Scott, M., Selvarajan, A., Paul, D., Skinner, D., Hanwell, M., Harris, C., Avery, P., Stezelberger, T., Tindall, C., Ramesh, R., Minor, A. & Denes, P. (2020). The 4D Camera – An 87 kHz Frame-rate Detector for Counted 4D-STEM Experiments. *Microscopy and Microanalysis* **26**, 1896–1897.

Guizar-Sicairos, M. & Fienup, J. R. (2008). Phase retrieval with transverse translation diversity: a nonlinear optimization approach. *Optics express* **16**, 7264–7278.

Haas, B., Schloz, M., Mittelberger, A., Lovejoy, T., Müller, J., Krivanek, O., Jones, L., Van den Broek, W. & Koch, C. (2020). Comparison of Ptychography vs. Center-of-mass Analysis of Registered 4D-

STEM Series. *Microscopy and microanalysis: the official journal of Microscopy Society of America, Microbeam Analysis Society, Microscopical Society of Canada* **26**, 1898–1900.

Hachtel, J. A., Idrobo, J. C. & Chi, M. (2018). Sub-Ångstrom electric field measurements on a universal detector in a scanning transmission electron microscope. *Advanced structural and chemical imaging* **4**, 10.

Heimes, D., Belz, J., Beyer, A. & Volz, K. (2020). Measuring Interatomic Bonding and Charge Redistributions in Defects by Combining 4D-STEM and STEM Multislice Simulations. *Microscopy and microanalysis: the official journal of Microscopy Society of America, Microbeam Analysis Society, Microscopical Society of Canada* **26**, 452–454.

Jannis, D., Hofer, C., Gao, C., Gao, X., Béché, A., Pennycook T. J. & Verbeeck J. (2021). *Event driven 4D STEM acquisition with a Timepix3 detector: microsecond dwell time and faster scans for high precision and low dose applications. Ultramicroscopy* **233**, 113423.

Jiang, Y., Chen, Z., Han, Y., Deb, P., Gao, H., Xie, S., Purohit, P., Tate, M. W., Park, J., Gruner, S. M., Elser, V. & Muller, D. A. (2018). Electron ptychography of 2D materials to deep sub-ångström resolution. *Nature* **559**, 343–349.

Jones, L. (2014). Scan-noise and Drift Correction in the STEM. *Microscopy today* **22**, 40–41.

Jones, L. & Nellist, P. D. (2013). Identifying and correcting scan noise and drift in the scanning transmission electron microscope. *Microscopy and microanalysis: the official journal of Microscopy Society of America, Microbeam Analysis Society, Microscopical Society of Canada* **19**, 1050–1060.

Jones, L., Wenner, S., Nord, M., Ninive, P. H., Løvvik, O. M., Holmestad, R. & Nellist, P. D. (2017). Optimising multi-frame ADF-STEM for high-precision atomic-resolution strain mapping. *Ultramicroscopy* **179**, 57–62.

Lazić, I., Bosch, E. G. T. & Lazar, S. (2016). Phase contrast STEM for thin samples: Integrated differential phase contrast. *Ultramicroscopy* **160**, 265–280.

Maiden, A. M., Humphry, M. J., Sarahan, M. C., Kraus, B. & Rodenburg, J. M. (2012). An annealing algorithm to correct positioning errors in ptychography. *Ultramicroscopy* **120**, 64–72.

Maiden, A. M. & Rodenburg, J. M. (2009). An improved ptychographical phase retrieval algorithm for diffractive imaging. *Ultramicroscopy* **109**, 1256–1262.

Müller-Caspary, K., Grieb, T., Müßener, J., Gauquelin, N., Hille, P., Schörmann, J., Verbeeck, J., Van Aert, S., Eickhoff, M. & Rosenauer, A. (2019). Electrical Polarization in AlN/GaN Nanodisks Measured by Momentum-Resolved 4D Scanning Transmission Electron Microscopy. *Physical review letters* **122**, 106102.

Müller, K., Krause, F. F., Béché, A., Schowalter, M., Galioit, V., Löffler, S., Verbeeck, J., Zweck, J., Schattschneider, P. & Rosenauer, A. (2014). Atomic electric fields revealed by a quantum

mechanical approach to electron picodiffraction. *Nature Communications* **5**, 5653.

Nguyen, K. X., Purohit, P., Hovden, R., Turgut, E., Tate, M. W., Kourkoutis, L. F., Fuchs, G. D., Gruner, S. M. & Muller, D. A. (2016). 4D-STEM for Quantitative Imaging of Magnetic Materials with Enhanced Contrast and Resolution. *Microscopy and Microanalysis* **22**, 1718–1719.

Ning, S., Fujita, T., Nie, A., Wang, Z., Xu, X., Chen, J., Chen, M., Yao, S. & Zhang, T.-Y. (2018). Scanning distortion correction in STEM images. *Ultramicroscopy* **184**, 274–283.

Nord, M., Webster, R. W. H., Paton, K. A., McVitie, S., McGrouther, D., MacLaren, I. & Paterson, G. W. (2020). Fast Pixelated Detectors in Scanning Transmission Electron Microscopy. Part I: Data Acquisition, Live Processing, and Storage. *Microscopy and Microanalysis* **26**, 653–666.

O'Leary, C. M., Allen, C. S., Huang, C., Kim, J. S., Liberti, E., Nellist, P. D. & Kirkland, A. I. (2020). Phase reconstruction using fast binary 4D STEM data. *Applied Physics Letters* **116**, 124101.

O'Leary, C., Haas, B., Koch, C., Nellist, P., & Jones, L. (2021). Increasing Spatial Fidelity and SNR of 4D-STEM Using Multi-Frame Data Fusion. *Microscopy and Microanalysis,* 1-11.

Ophus, C. (2019). Four-Dimensional Scanning Transmission Electron Microscopy (4D-STEM): From Scanning Nanodiffraction to Ptychography and Beyond. *Microscopy and microanalysis: the official journal of Microscopy Society of America, Microbeam Analysis Society, Microscopical Society of Canada* **25**, 563–582.

Ophus, C., Ercius, P., Sarahan, M., Czarnik, C. & Ciston, J. (2014). Recording and Using 4D-STEM Datasets in Materials Science. *Microscopy and microanalysis: the official journal of Microscopy Society of America, Microbeam Analysis Society, Microscopical Society of Canada* **20**, 62–63.

Pelz, P. M., Qiu, W. X., Bücker, R., Kassier, G. & Miller, R. J. D. (2017). Low-dose cryo electron ptychography via non-convex Bayesian optimization. *Scientific Reports* **7**, 9883.

Pennycook, S. J. (2017). The impact of STEM aberration correction on materials science. *Ultramicroscopy* **180**, 22–33.

Pennycook, T. J., Lupini, A. R., Yang, H., Murfitt, M. F., Jones, L. & Nellist, P. D. (2015). Efficient phase contrast imaging in STEM using a pixelated detector. Part 1: experimental demonstration at atomic resolution. *Ultramicroscopy* **151**, 160–167.

Pennycook, T. J., Martinez, G. T., Nellist, P. D., & Meyer, J. C. (2019). High dose efficiency atomic resolution imaging via electron ptychography. *Ultramicroscopy*, **196**, 131–135.

Plackett, R., Horswell, I., Gimenez, E. N., Marchal, J., Omar, D. & Tartoni, N. (2013). Merlin: a fast versatile readout system for Medipix3. *Journal of Instrumentation* **8**, C01038.

Rodenburg, J. & Maiden, A. (2019). Ptychography. *Springer Handbook of Microscopy*.

Savitzky, B. H., Zeltmann, S. E., Hughes, L. A., Brown, H. G., Zhao, S., Pelz, P. M., Pekin, T. C., Barnard, E. S., Donohue, J., Rangel DaCosta, L., Kennedy, E., Xie, Y., Janish, M. T., Schneider, M.

M., Herring, P., Gopal, C., Anapolsky, A., Dhall, R., Bustillo, K. C., Ercius, P., Scott, M. C., Ciston, J., Minor, A. M. & Ophus, C. (2021). py4DSTEM: A Software Package for Four-Dimensional Scanning Transmission Electron Microscopy Data Analysis. *Microscopy and microanalysis: the official journal of Microscopy Society of America, Microbeam Analysis Society, Microscopical Society of Canada* **27**, 712–743.

Shenfield, A. & Rodenburg, J. M. (2011). Evolutionary determination of experimental parameters for ptychographical imaging. *Journal of Applied Physics* **109**, 124510.

Tinti, G., Fröjdh, E., van Genderen, E., Gruene, T., Schmitt, B., de Winter, D. A. M., Weckhuysen, B. M. & Abrahams, J. P. (2018). Electron crystallography with the EIGER detector. *IUCrJ* **5**, 190–199.

Wen, Y., Ophus, C., Allen, C. S., Fang, S., Chen, J., Kaxiras, E., Kirkland, A. I. & Warner, J. H. (2019). Simultaneous Identification of Low and High Atomic Number Atoms in Monolayer 2D Materials Using 4D Scanning Transmission Electron Microscopy. *Nano letters* **19**, 6482–6491.

Xu, W., Lin, H., Wang, H. & Zhang, F. (2020). Reconstruction method of a ptychographic dataset with unknown positions. *Optics letters* **45**, 4634–4637.

Yang, H., Jones, L., Ryll, H., Simson, M., Soltau, H., Kondo, Y., Sagawa, R., Banba, H., MacLaren, I. & Nellist, P. D. (2015). 4D STEM: High efficiency phase contrast imaging using a fast pixelated detector. *Journal of physics. Conference series* **644**, 012032.

Yang, H., Pennycook T.J. & Nellist, P. D. (2015). Efficient phase contrast imaging in STEM using a pixelated detector. Part II: optimisation of imaging conditions. Ultramicroscopy, 151, 232–239.

Yang, H., Rutte, R. N., Jones, L., Simson, M., Sagawa, R., Ryll, H., Huth, M., Pennycook, T. J., Green, M. L. H., Soltau, H., Kondo, Y., Davis, B. G. & Nellist, P. D. (2016). Simultaneous atomic-resolution electron ptychography and Z-contrast imaging of light and heavy elements in complex nanostructures. *Nature Communications* **7**, 12532.

Zhang, F., Peterson, I., Vila-Comamala, J., Diaz, A., Berenguer, F., Bean, R., Chen, B., Menzel, A., Robinson, I. K. & Rodenburg, J. M. (2013). Translation position determination in ptychographic coherent diffraction imaging. *Optics express* **21**, 13592–13606.

Zhou, L., Song, J., Kim, J. S., Pei, X., Huang, C., Boyce, M., Mendonça, L., Clare, D., Siebert, A., Allen, C. S., Liberti, E., Stuart, D., Pan, X., Nellist, P. D., Zhang, P., Kirkland, A. I. & Wang, P. (2020). Low-dose phase retrieval of biological specimens using cryo-electron ptychography. *Nature communications* **11**, 2773.

Supporting Materials

Accurate and Robust Calibration of the Uniform Affine Transformation Between Scan-Camera coordinates for Atom-Resolved In-Focus 4D-STEM Datasets

Shoucong Ning[1, 2], Wenhui Xu[3, 4], Yinhang Ma[5], Leyi Loh[1], Timothy J. Pennycook[6], Wu Zhou[5], Fucai Zhang[3], Michel Bosman[1], Stephen J. Pennycook[5], Qian He[1]*, N. Duane Loh[2,7,8]*

1. Department of Materials Science and Engineering, National University of Singapore, 117575, Singapore
2. Center for Bio-Imaging Sciences, National University of Singapore, 117557, Singapore.
3. Department of Electrical and Electronic Engineering, Southern University of Science and Technology, Shenzhen 518055, China
4. Harbin Institute of Technology, Harbin, 150001, China
5. School of Physical Sciences and CAS Key Laboratory of Vacuum Physics, University of Chinese Academy of Sciences, Beijing, 100049, China
6. EMAT, Universiteit Antwerpen, Campus Groenenborger, 2020 Antwerpen, Belgium
7. Department of Physics, National University of Singapore, 117551, Singapore.
8. Department of Biological Sciences, National University of Singapore, 117557, Singapore.

Table of Contents

S1 Coordinate system transformation between the J_{scan} and the J_{det} matrices

Using the camera coordinates that is Cartesian as a reference, if the scanning coordination system has been uniformly rotated for an angle θ, then

$$\boldsymbol{h} = (\cos\theta\,, \sin\theta) * \Delta$$
$$\boldsymbol{v} = (-\sin\theta\,, \cos\theta) * \Delta$$

where $\boldsymbol{h}$ is the fast-scanning direction, and $\boldsymbol{v}$ is the slow scanning direction, Δ is the scan interval in the sample plane and the scan interval along the fast and slow scanning direction is assumed to be the same for a conventional raster scanning. In the reciprocal space, we have:

$$\boldsymbol{k_h} = (\cos\theta\,, \sin\theta)/\Delta$$
$$\boldsymbol{k_v} = (-\sin\theta\,, \cos\theta)/\Delta$$

where $\boldsymbol{k_h}$ and $\boldsymbol{k_v}$ is the corresponding reciprocal vectors of $\boldsymbol{h}$ and $\boldsymbol{v}$, respectively. Using the chain rule, the gradient of a E_x components of the electric field along the horizontal direction of the camera coordinates is formulated as:

$$\frac{\partial E_x}{\partial x} = \frac{\partial E_x}{\partial h} * \frac{\partial h}{\partial x} + \frac{\partial E_x}{\partial v} * \frac{\partial v}{\partial x} = \Delta\frac{\partial E_x}{\partial h} * \cos\theta - \Delta\frac{\partial E_x}{\partial v} * \sin\theta$$
$$\frac{\partial E_x}{\partial y} = \frac{\partial E_x}{\partial h} * \frac{\partial h}{\partial y} + \frac{\partial E_x}{\partial v} * \frac{\partial v}{\partial y} = \Delta\frac{\partial E_x}{\partial h} * \sin\theta + \Delta\frac{\partial E_x}{\partial v} * \cos\theta$$

The E_y component of the electric field E along the vertical direction of the camera coordinate can be formulated in the same way.

$$\frac{\partial E_y}{\partial x} = \frac{\partial E_y}{\partial h} * \frac{\partial h}{\partial x} + \frac{\partial E_y}{\partial v} * \frac{\partial v}{\partial x} = \Delta\frac{\partial E_y}{\partial h} * \cos\theta - \Delta\frac{\partial E_y}{\partial v} * \sin\theta$$
$$\frac{\partial E_y}{\partial y} = \frac{\partial E_y}{\partial h} * \frac{\partial h}{\partial y} + \frac{\partial E_y}{\partial v} * \frac{\partial v}{\partial y} = \Delta\frac{\partial E_y}{\partial h} * \sin\theta + \Delta\frac{\partial E_y}{\partial v} * \cos\theta$$

Rewrite above equations for both E_x and E_y as a matrix multiplication:

$$\begin{bmatrix} \frac{\partial E_x}{\partial x} & \frac{\partial E_y}{\partial x} \\ \frac{\partial E_x}{\partial y} & \frac{\partial E_y}{\partial y} \end{bmatrix} = \Delta \begin{bmatrix} \cos\theta & -\sin\theta \\ \sin\theta & \cos\theta \end{bmatrix} \begin{bmatrix} \frac{\partial E_x}{\partial h} & \frac{\partial E_y}{\partial h} \\ \frac{\partial E_x}{\partial v} & \frac{\partial E_y}{\partial v} \end{bmatrix}$$

where E_x and E_y are the electric field components determined from the diffraction patterns in the camera coordinates. $\begin{bmatrix} \frac{\partial E_x}{\partial h} & \frac{\partial E_y}{\partial h} \\ \frac{\partial E_x}{\partial v} & \frac{\partial E_y}{\partial v} \end{bmatrix}$ can be numerically computed for each scanning position.

S2 STEM image simulation parameters.

The simulated datasets shown in **Figures 1**, **2, 3, S3, 5, and 8** are generated using the same sample and same machine parameters. The defocus is set to 0. The accelerating voltage is set to 80 kV, the probe forming lens aperture is set to 30mrad, and the size of the electron probe is set to 256*256 pixels. The maximum angle of the diffraction patterns is set to 120 mrad, indicating a 44.6Å sptial extend and a 0.17 Å sampling interval of the probe. In the simulated data used in **Figure 8**, the aperture is reduced to 24 mrad, and the pixel number and spatial extend of the probe is the same as **Figure1** (**b-e**). The CUDAEM code developed by Dr. Ning is used for the simulations, the slice thickness is set to 0.5 Å, and the phonon configuration number is set to 80 to consider the thermal diffuse scattering. **Figure2 III** and **Figure3** share the same simulation parameters except for probe-forming lens settings to consider residual lens aberrations.

In the simulation of the 4D-STEM dataset of thick MoS_2 sample shown in **Figure 7** and **Figure S9**, the accelerating voltage, the probe forming lens aperture and the size of the electron probe are kept the same as monolayer MoS_2. The slice thickness is set to 0.5 angstroms, and the number of phonon configurations is set to 40. As shown in **Figure S1**, compared to the position averaged CBED (PACBED) of the monolayer MoS_2, the boundary of the bright field aperture of thick MoS_2 with 30nm thickness is interrupted due to the multiple scattering.

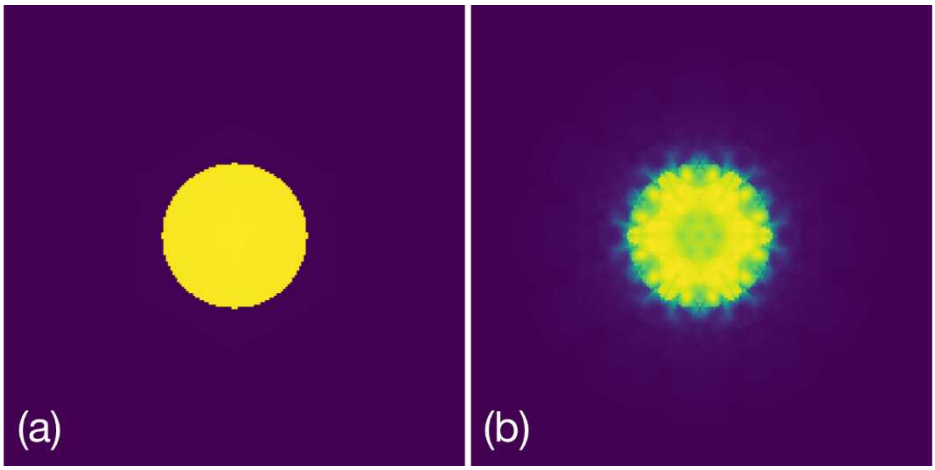

Figure S1. The averaged CBED patterns of (**a**) monolayer MoS_2 and (**b**) 30nm thick MoS_2.

S3 The selection of target functions in the J-matrix method.

The published method (Hachtel et al., 2018) identifies the uniform rotation angle by either maximizes the charge density or minimizes the curls of the electric field, which are mathematically equivalent. In the *J-matrix method*, the sum of the difference between the squared diagonal terms (charge density) and non-diagonal terms (curls) are combined as one target function in the determination of the uniform rotation angle θ in order to improve the signal to noise ratio in practice. The Jacobian matrix J_{det} computed in the camera coordinates is given in **EQ2** in the main text as:

$$J_{det} = \Delta \begin{bmatrix} \cos\theta & -\sin\theta \\ \sin\theta & \cos\theta \end{bmatrix} J_{scan} = \begin{bmatrix} J_1' & J_2' \\ J_3' & J_4' \end{bmatrix}$$

where $J_{scan} = [J_1, J_2; J_3, J_4]$ is numerically computed in the coordinate system of the scanning coordinate system for each scanning position. Assuming $\Delta = 1$ (Δ does not influence the determination of rotation angle), the sums of each squared diagonal at all scanning position is:

$$\sum {J_1'}^2 = \sum (J_1 \cos\theta - J_3 \sin\theta)^2 = \sum J_1^2 \cos^2\theta + J_3^2 \sin^2\theta - 2J_1J_3 \cos\theta \sin\theta$$

$$\sum {J_4'}^2 = \sum (J_2 \sin\theta + J_4 \cos\theta)^2 = \sum J_4^2 \cos^2\theta + J_2^2 \sin^2\theta + 2J_2J_4 \cos\theta \sin\theta$$

Then the sums of the squared diagonal at all scanning position is:

$$\sum ({J_1'}^2 + {J_4'}^2) = \sum (J_1^2 + J_4^2) \cos^2\theta + (J_2^2 + J_3^2) \sin^2\theta + 2(J_2J_4 - J_1J_3) \cos\theta \sin\theta$$

Since $2\cos\theta \sin\theta = \sin 2\theta$, $\cos^2\theta = (\cos 2\theta + 1)/2$, $\sin^2\theta = (1 - \cos 2\theta)/2$, the above equation will be updated as:

$$\sum ({J_1'}^2 + {J_4'}^2) = \sum (J_1^2 + J_4^2)(\cos 2\theta + 1)/2 + (J_2^2 + J_3^2)(1 - \cos 2\theta)/2 + (J_2J_4 - J_1J_3) \sin 2\theta$$

A simple form will be derived by separating the constant and variates:

$$\sum ({J_1'}^2 + {J_4'}^2) = cos2\theta \frac{\sum (J_1^2 + J_4^2 - J_2^2 - J_3^2)}{2} + sin\ 2\theta \sum (J_2J_4 - J_1J_3) + \sum (J_1^2 + J_2^2 + J_3^2 + J_4^2)\ /2$$

Similarly, the integrated squared non-diagonal terms of J_{det} at rotation angle θ at all scanning positions is:

$$\sum({J'_2}^2 + {J'_3}^2) = cos2\theta \sum \frac{(J_2^2 + J_3^2 - J_1^2 - J_4^2)}{2} + sin\ 2\theta \sum (J_1 J_3 - J_2 J_4)$$
$$+ \sum (J_1^2 + J_2^2 + J_3^2 + J_4^2)\ /2$$

Consequently, maximizing the squared diagonal terms or minimizing the squared non-diagonal terms are equivalent. Practically, in order to improve the signal to noise ratio, both the charge density and the curl are used in the J-matrix method as the target function $T(\theta)$ to determine the uniform rotation angle θ:

$$\mathrm{T}(\theta) = \sum({J'_1}^2 + {J'_4}^2) - \sum({J'_2}^2 + {J'_3}^2)$$
$$= -\ cos\ 2\theta \sum (J_2^2 + J_3^2 - J_1^2 - J_4^2) + 2sin\ 2\theta \sum (J_2 J_4 - J_1 J_3)$$

When $\partial T(\theta)/\partial\theta$ equals zero, the uniform rotation angle θ is analytically given as **EQ3** in the main text:

$$tan2\theta = 2\sum (J_2 J_4 - J_1 J_3)\ /\ \sum (J_1^2 + J_4^2 - J_2^2 - J_3^2)$$

S4 Influence of chirality change on ptychography reconstruction.

To show the influence of incorrect initialization of scanning positions, the simulated 4D STEM dataset of single-layered graphene is used. The whole dataset consists of 64*64*256*256 pixels, the defocus and aperture of the probe are set to 40nm and 30 mrad, respectively. The accelerating voltage is 60 kV, and the maximum angle in the diffraction pattern is set to 120 mrad, indicating a 0.2 Å sampling interval. There is no rotation between the CBED frames and scanning positions of the probe. The scanning interval along both directions is 0.65 angstroms, and this interval ensures the uniqueness of reconstructed results. The ePIE approach (Maiden & Rodenburg, 2009) is adopted in the reconstruction of the object and electron probe, and only the bright field signal of CBED patterns is used. The reconstructed object has almost no changes after 100 iterations; the phase angle of the reconstructed result is plotted in **Figure S2** (**a**). As shown, the phase distribution of carbon atoms inside the scanned area matches the atomic structures of graphene. The outline of the atomic model is successfully retrieved, and an extension of this model is also observed due to the periodic boundary condition adopted in the multislice simulation. When a π-rotation is applied to the scanning positions, the reconstructed object phase distribution (**Figure S2** (**b**)) shows inverted contrast compared to **Figure S2** (**a**). The negative phase values at carbon atoms consist of the electric field in **Figure 1** (**e**). In **Figure S2**(**c**), further ptychography reconstruction is conducted with flipped fast scanning direction and the determined object phase is shown. Different from the π-rotation case, there are almost no similarities between **Figure S2**(**a**) and **Figure S2**(**c**), the structure of graphene cannot be correlated with the reconstructed phase when the chirality of the scanning directions is changed.

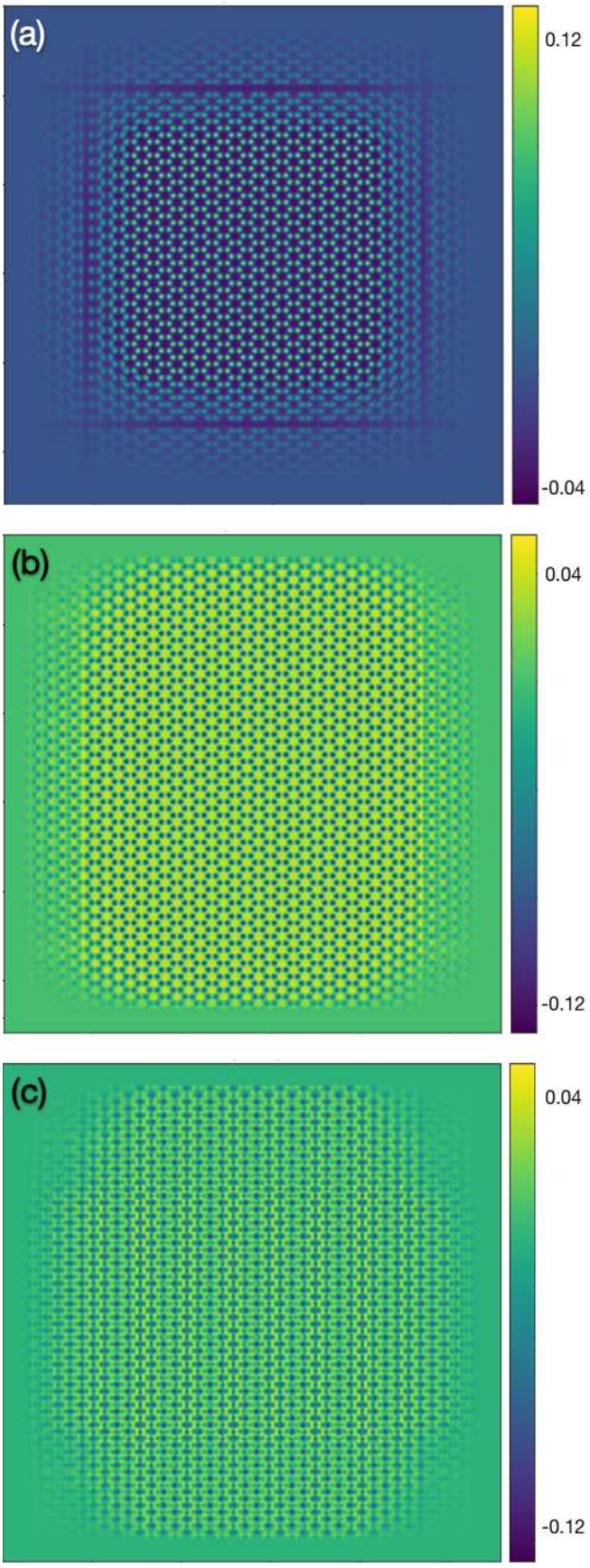

Figure S2. Ptychography reconstruction phase results using different scanning directions based on a simulated graphene 4D STEM dataset. (**a**). Reconstructed phase angle when the diffraction patterns are flipped and the scanning vectors are determined directly on modified diffraction patterns. (**b**). Reconstructed phase angle when the scanning vectors along the row and column direction are rotated by 180° referring to their correct values. (**c**). Reconstructed phase angle when the flip is applied to diffraction patterns but the corresponding probe positions of these diffraction patterns are the same as the values used in the simulation. Color bars represent the phase shift in the unit of radian. The accelerating voltage used in the simulation was 60kV**.**

S5 About the Weighted J-Matrix.

The weighted Jacobian matrix J_w of the electric field is used to ensure the solution uniqueness of the *J-matrix method* and check the existence of the flip, and the weight used in the generation of J_w is the signal having higher values at nuclei. Taking the simulated 4D-STEM dataset of monolayer MoS2 given in Figure 2(i) as an example. The ADF-STEM image of it is chosen as the weight matrix, and J_w is computed by multiplying the ADF intensity at each scanning position with the terms of *J-matrix*. The integrated J_w at all scanning positions at rotation angles 0° and 180° are listed in Table S1. At angle 0°, both two diagonal terms are positive, and they are right opposite to the 180° case. In comparison, the corresponding integrated squared *J-matrix* listed in Table S2 does not show any difference when the 180° rotation is applied.

J_w terms	J1	J2	J3	J4
0°	2469.93	1.25	1.14	2504.16
180°	-2469.93	-1.25	-1.14	-2504.16
Horizontal flip	-2469.93	1.25	-1.14	2504.16

Table S1. The integrated terms of weighted Jacobian matrix at different geometrical configurations.

J terms	J1	J2	J3	J4
0°	11547.11	4296.81	4296.81	11547.11
180°	11547.11	4296.81	4296.81	11547.11
Horizontal flip	11547.11	4296.81	4296.81	11547.11

Table S2. The integrated terms of the squared Jacobian matrix at different geometrical configurations.

Moreover, when the fast scanning direction ***h*** is flipped, the gradient of the electric field along this direction will become their negative values. As listed in **Table S1**, the two diagonal terms show different signs at rotation angles 0 and 180°, while the flip does not have any influences on the integrated terms of the squared *J-matrix* as shown in **Table S2**. Consequently, the *weighted J-matrix* J_w must be computed to detect the flip and find the unique solution.

The flip of the scanning directions does not influence the determination of uniform rotation angle computed using **EQ3** since the square of gradient terms listed in **Table S2** is used. Consequently,

we use **EQ3** to determine the possible uniform rotation angles in practice. Then the integrated squared Jacobian matrix will be computed at these angles to exclude the two solutions. After that, the only solution and possible flip can be confirmed when integrated J_w is known.

S6 Other factors influencing the accuracy of the J-matrix method.

In addition to the sampling interval, lens aberrations, and scanning distortions, other factors such as camera tilt, camera gain distribution, point spread function (PSF), incoherency, and the sample thickness are also evaluated in this part. In **Figure S3** (**a**) and (**b**), a 10° rotation is applied to the electron camera and the vertical direction is taken as the rotational axis. Compared to the result computed in **Figure 3** (**a**) and (**b**), the tilt of the cameras do not influence the accuracy of the *J-matrix method*. Moreover, the other properties of cameras such as PSF (**Figure S3**(**g**)) and gain distribution (**Figure S3** (**c**) and (**d**)) also have negligible influence on the determined rotation angle. The incoherency of the electron microscope reduces the error by enhancing the spatial continuity of the electric field since the spatial resolution of the electron probe decreases. In addition, the temporal incoherence (**Figure S3** (**f**)) has smaller influences on the accuracy compared to the spatial incoherent case (**Figure S3** (**e**)) although the contrast of its CBED patterns has been more dramatically reduced. The surprising result appears when the sample thickness is considered as shown in **Figure S3** (**h**) and (**i**). The increasing sample thickness reduces the error caused by the *J-matrix method* when a 25° rotation was applied to the CBED patterns. The dynamical scattering of the electrons in the thick specimen possibly eliminates the difference of properties of the computed electric field in both scanning directions.

To further explore the factors causing the error at the case with a 25° rotation, we rotate the CBED patterns in the dataset shown in **Figure 2**. **I** and **IV** from 0° to 45° with a 5° interval. As shown in **Table S3**, for both datasets, the computed angle obviously increases as the rotation angle increases, and symmetrically drops off at 45°. For the dataset with a 0.34Å scan interval, the angular error is more dramatic compared to the 0.17Å case. Consequently, the angular error is caused by the interruption of continuity of the electric field, and this error is a function of both rotation angle and the scan interval. The error disappears at 45° since the errors along the horizontal and the vertical direction cancel each other.

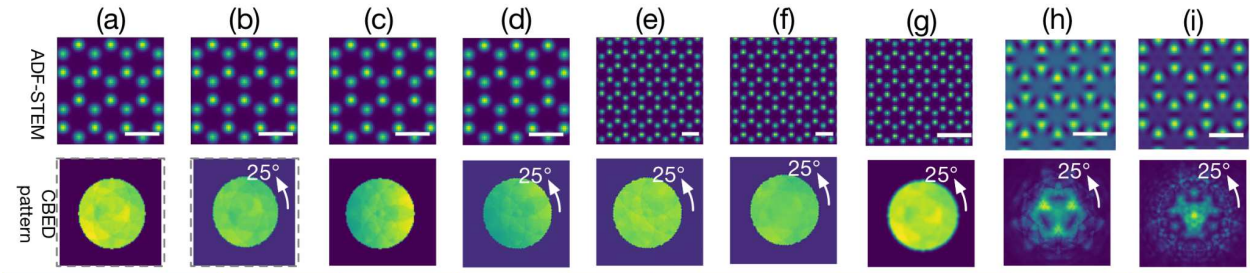

frame ID	(a)	(b)	(c)	(d)	(e)	(f)	(g)	(h)	(i)
true rotation angle	0°	25°	0°	25°	25°	25°	25°	25°	25°
detector tilt	Y	Y	N	N	N	N	N	N	N
scan step size	0.17Å	0.17Å	0.17Å	0.17Å	0.34Å	0.34Å	0.34Å	0.17Å	0.17Å
spatial incoherency	N	N	N	N	Y	N	N	N	N
temporal incoherency	N	N	N	N	N	Y	N	N	N
detector gain	N	N	Y	Y	N	N	N	N	N
sample thickness	3.0Å	3.0Å	3.0Å	3.0Å	3.0Å	3.0Å	3.0Å	15 nm	30 nm
PSF	N	N	N	N	N	N	Y	N	N
compute angle	-0.03°	26.02°	-0.03	26.02°	29.68°	30.36°	30.40°	24.66°	25.13°
angle error	0.03°	1.02°	0.72°	1.02°	4.68°	5.36°	5.40°	0.34°	0.13°

Figure S3. The influence of extra factors on the accuracy of the *J-matrix method*. (**a**-**b**) The camera is rotated by 10° along the vertical direction to consider the camera tilt. In (**b**), CBED patterns are rotated by 25° to introduce the sampling artifacts and differences of the electric field along with the horizontal and vertical directions. (**c**-**d**). The gain distribution of the camera is considered by applying a gain distribution function linearly increasing along the horizontal direction. As shown by the CBED patterns, the intensity is lower on the left part since the gain on the left is 0.4 and grows to 0.6 on the right border of the aperture. In (**d**), A 25° rotation is also applied. (**e**-**f**) The spatial and temporal incoherence is considered in the 4D-STEM simulation, the defocus spread is set to 4.88nm and the source size is set to 0.37 angstroms. In addition, the scanning step size is set to 0.34 angstroms for both cases. (**g**) The point spread function of the camera is considered by the convolution of CBED patterns with a Gaussian kernel, and the sigma value of the Gaussian kernel is set to 1.0 pixel. The scanning step size is the same as (**e**) and (**f**). In (**h**) and (**i**), the thickness of the sample increases to 15 nm and 30 nm, respectively, and the scanning step size is set to 0.17 angstroms. In addition, the CBED patterns are rotated by 25° to evaluate if the sample thickness can suppress the sampling artifacts and differences of the electric field in each scanning direction. The scale bars represent 3.0 Å. The accelerating voltage used in the simulation was 80kV and more details can be found in **Supporting Materials S2.**

Step size	0°	5°	10°	15°	20°	25°	30°	35°	40°	45°
0.34Å	0.02°	2.42°	4.32°	5.47°	5.78°	5.41°	4.49°	3.20°	1.66°	0.01°
0.17Å	0.01	0.41°	0.71°	0.94°	1.04°	1.02°	0.88°	0.65°	0.34°	0.01°

Table S3. The influence of CBED rotation angles on the difference between the true rotation angle and computed rotation angle using the *J-matrix method* at 0.17 Å and 0.34Å scanning step size. As the rotation angle increases, the error increases and starts to drop off around 22.5°, and finally reduces to near zero at 45°. This phenomenon is due to the different properties of the electric field in different scanning directions and sampling artifacts.

S7. First-order disk shift vector Q.

Following the discussion in the section **S1**, the shift vector $\boldsymbol{Q}$ of the first order disks relative to the center disk in the G-slices with index *(i, j)* according to $\boldsymbol{k_h}$ and $\boldsymbol{k_v}$ is given as:

$$\boldsymbol{Q} = i\boldsymbol{k_h} + j\,\boldsymbol{k_v} = (i * \cos\theta - j * \sin\theta\,, i * \sin\theta + j * \cos\theta)/\Delta$$

When the rotation angle and scanning interval are not uniform, we assume that there is an affine transformation between the scanning positions and the camera. Then the real space and reciprocal space vector of scanning directions are given as:

$$\boldsymbol{h} = (\cos\theta_x\,, \sin\theta_x) * \Delta$$

$$\boldsymbol{v} = (-\sin\theta_y\,, \cos\theta_y) * \gamma\Delta$$

In reciprocal space, the corresponding reciprocal space scanning frequency is:

$$\boldsymbol{k_h} = (\cos\theta_y\,, \sin\theta_y)/(\Delta')$$

$$\boldsymbol{k_v} = (-\sin\theta_x\,, \cos\theta_x)\gamma/(\Delta')$$

$$\Delta' = \Delta(\cos\theta_y \cos\theta_x + \sin\theta_x \sin\theta_y)$$

where θ_x, θ_y are the rotation angle of the fast and slow scanning direction, respectively. Δ' equals Δ only when $\theta_x = \theta_y$ due to the reciprocal relationship. The relationship between the Jacobian Matrix computed in scanning coordinate systems and camera coordinate systems is modified as:

$$\begin{bmatrix} \frac{\partial E_x}{\partial x} & \frac{\partial E_y}{\partial x} \\ \frac{\partial E_x}{\partial y} & \frac{\partial E_y}{\partial y} \end{bmatrix} = \Delta \begin{bmatrix} \cos\theta_x & -\gamma \sin\theta_y \\ \sin\theta_x & \gamma \cos\theta_y \end{bmatrix} \begin{bmatrix} \frac{\partial E_x}{\partial h} & \frac{\partial E_y}{\partial h} \\ \frac{\partial E_x}{\partial v} & \frac{\partial E_y}{\partial v} \end{bmatrix}$$

The shift vector $\boldsymbol{Q}$ of the first order disks relative to the center disk in the G-slices with index *(i, j)* is given as:

$$\boldsymbol{Q} = (i * cos\ \theta_y\ - j * \gamma sin\ \theta_x\ , i * sin\ \theta_y\ + j * \gamma cos\ \theta_x\ )/\Delta'$$

S8. The Algorithm of fitting first-order disks.

S7.1 Disk fitting algorithm

In the G-set slices of Fourier transformed 4D-STEM datasets, three disks including the direct disk and two first-order appear. The direct disk shares the same position with the aperture, and the other two first-order disks are relatively shifted referring to the direct disk with the opposite shift vectors $\boldsymbol{Q}$ and -$\boldsymbol{Q}$. Here we proposed an algorithm to accurately determine the first order disk, or the shift vector $\boldsymbol{Q}$ by maximizing the similarity between the slice and the predicted slice using $\boldsymbol{Q}$. For weak-phase objects, the non-overlapped area of these disks shows zero intensities. When there are almost no aberrations in the probe forming lens, the triple overlapped areas show zero intensities. When the residual aberrations appear, the intensity distribution inside the triple overlapped area cannot be easily predicted.

To estimate the intensity distribution after computing the shift vector of first-order disks using known geometric parameters, the bright field disk (**Figure S4.** (**a**)) is shifted with this vector and its inversion. The shifted frames (**Figure S4.** (**b-c**)) are summed and multiplied with the bright field disk to generate the intensity distribution of G-set slices as shown in **Figure S4.** (**d**). If there is no residual aberration, the triple overlapped region (the brightest part in **Figure S4.** (**d**)) can be set to zero. Now we can generate the ideal intensity distribution of G-set slices when $\boldsymbol{Q}$ is known as shown in **Figure S4**.

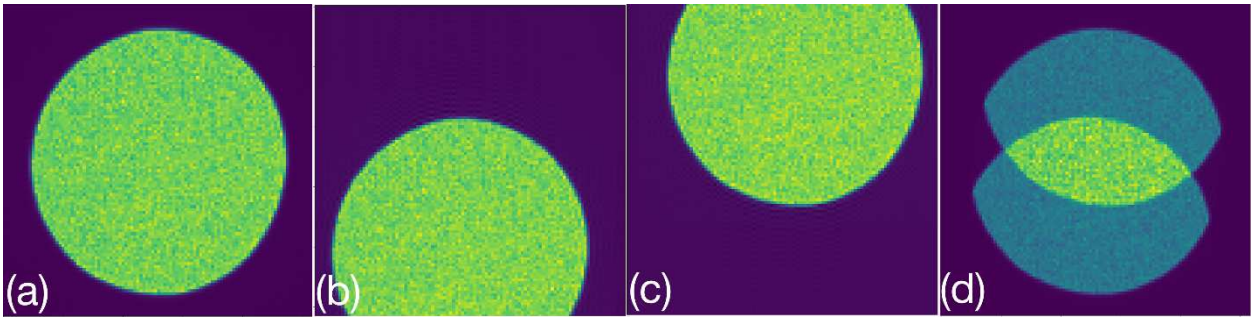

Figure S4. The generation of the intensity distribution in a G-set slice. (**a**) The zero-order disk, or the bright field disk. (**b-c**) The first-order disks determined using the provided disk shift vector, or the probe frequency vector computed using the geometric parameters and slice index. (**d**) Estimated intensity distribution in the G-set slice by summing (**b**) and (**c**), and masking with (**a**).

Using the cross-correlation between the intensity distribution of actual and estimated G-set slices (**Figure S5.** (**a-b**)) as the objective function, the $\boldsymbol{Q}$, or the geometric parameters can be estimated iteratively using various optimization methods. The initialization of $\boldsymbol{Q}$ can be done manually or using the geometric parameters determined using the *J-matrix method*. Practically, we can select the slices with high spatial frequencies to get rid of the triple overlapped region. For the cases when the triple overlapped region appears in the G-set slices and the intensity distribution in this region varies, the gradient error between the actual and estimated G-set slices (**Figure S5.** (**c-d**)) can be used as the to be minimized target when optimizing $\boldsymbol{Q}$.

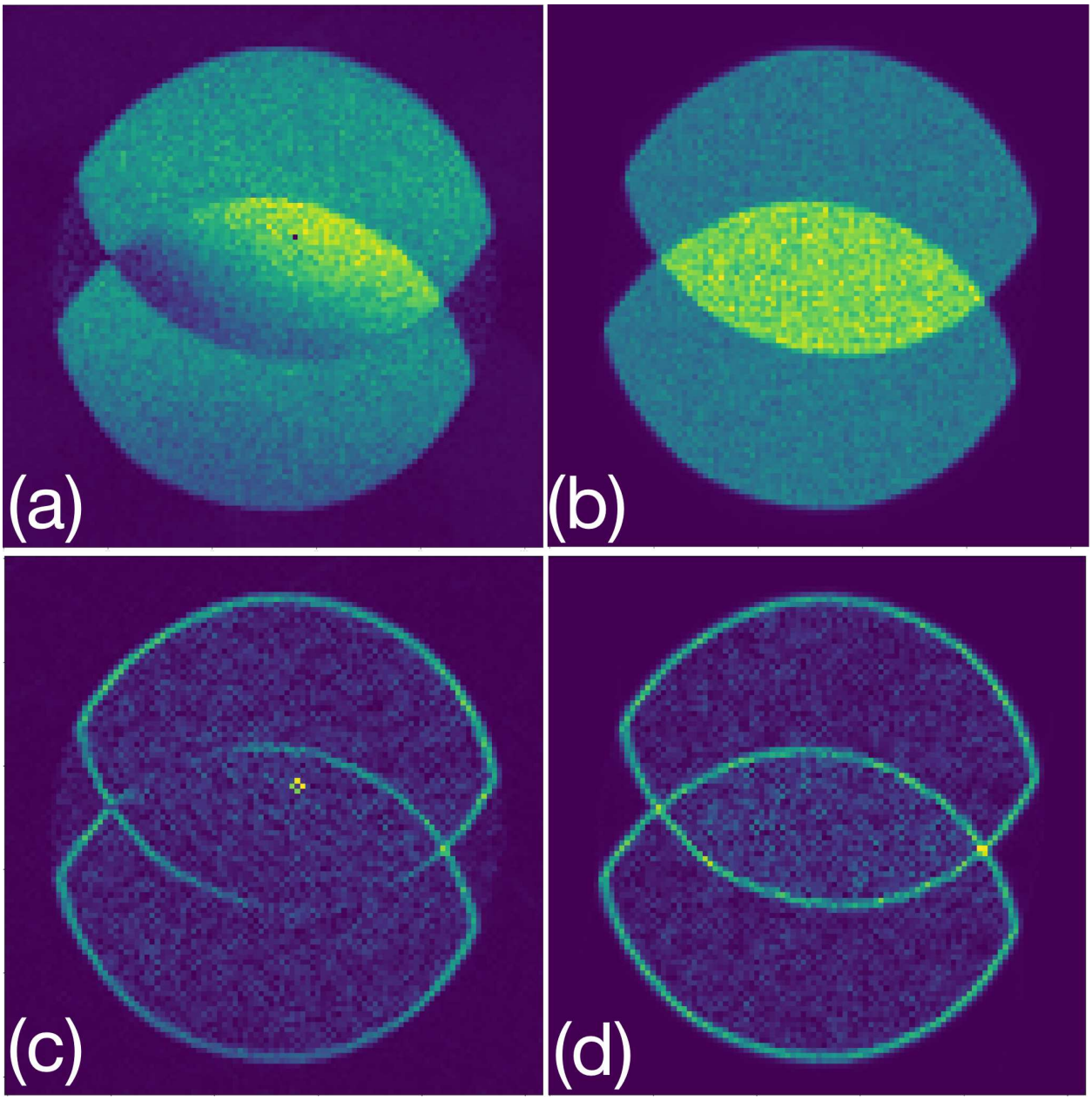

Figure S5. (**a**) Experimental G-set slice with index (i = 6, j=20). (**b**) Generated G-set slice using the refined geometric parameters. (**c**) Gradient of (**a**). (**d**) Gradient of (**b**).

S7.2 Procedures of the Fourier method

To get a better understanding of our *Fourier method* and its source code, the procedures of the *Fourier method* are given as follows.

1. Generate the position averaged CBED patterns on the 4D-STEM dataset and locate the center of the position averaged CBED pattern.

2. Trim the diffraction patterns of 4D-STEM dataset. The aperture must be included in the trimmed dataset, and the center of the position averaged CBED corresponds to the center of each trimmed diffraction pattern.
3. Apply Fourier transformation on the trimmed 4D-STEM dataset with respect to scan coordinates.
4. Plot the total intensity distribution on different probe frequencies, and select three slices in the G-sets with large total intensity values.
5. Determine the $\boldsymbol{Q}$ vectors in the selected slices using the disk fitting algorithm.
6. Compute the geometric parameters such as θ_x, θ_y, Δ' and γ with the $\boldsymbol{Q}$ vectors of slices of the G-sets and their corresponding frequency index (i, j) by solving these equation groups:

$$\begin{cases} i_1 * \Delta^{'} \cos\ \theta_y - j_1 * \gamma\Delta^{'} \sin\theta_x = Q_{x1} \\ i_2 * \Delta^{'} \cos\ \theta_y - j_2 * \gamma\Delta^{'} \sin\theta_x = Q_{x2} \\ i_3 * \Delta^{'} \cos\ \theta_y - j_3 * \gamma\Delta^{'} \sin\theta_x = Q_{x3} \end{cases}$$

$$\begin{cases} i_1 * \Delta^{'} \sin\theta_y + j_1 * \gamma\Delta^{'} \cos\theta_x = Q_{y1} \\ i_2 * \Delta^{'} \sin\theta_y + j_2 * \gamma\Delta^{'} \cos\theta_x = Q_{y2} \\ i_3 * \Delta^{'} \sin\theta_y + j_3 * \gamma\Delta^{'} \cos\theta_x = Q_{y3} \end{cases}$$

Where Q_x and Q_y are the horizontal and the vertical components of $\boldsymbol{Q}$, respectively. The i_1, i_2, i_3 are the horizontal index of three slices, and j_1, j_2, j_3 are their vertical indexes. From these two equation groups, the $\Delta' \cos\ \theta_y$, $\Delta' \sin\theta_y$ and $\gamma\Delta^{'} \sin\theta_x$, $\gamma\Delta^{'} \cos\theta_x$ can be solved firstly. Then θ_x, θ_y are known. Then the Δ' and γ can be determined by solving these six linear equations with the least square method. When θ_x, θ_y and Δ' are known, Δ can be solved using the following relationship:

$$\Delta^{'} = \Delta(\cos\theta_y \cos\theta_x + \sin\theta_x \sin\theta_y)$$

S9 The reconstructed object using different aberration correction results.

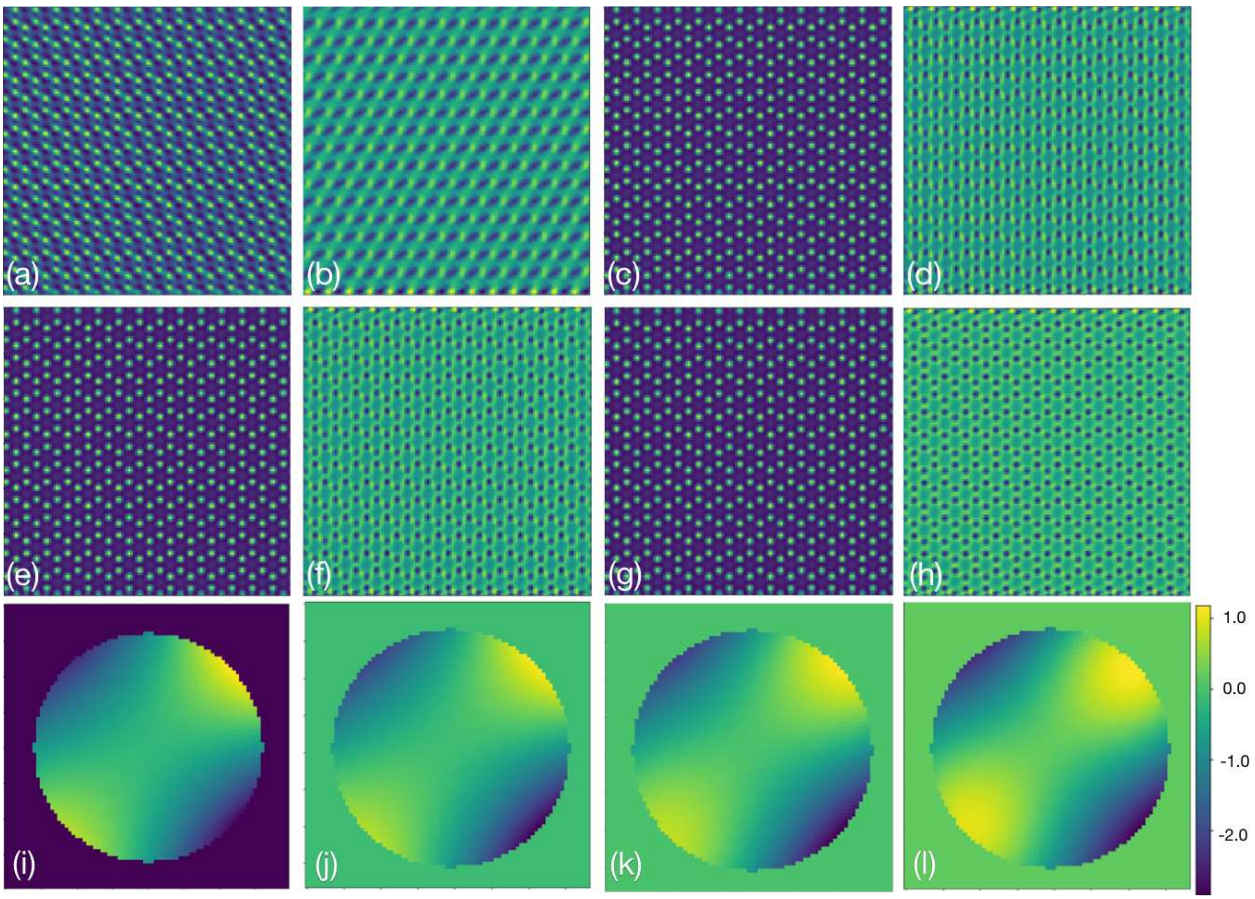

Figure S6. Reconstructed object functions using SSB methods on the simulated dataset **VI** shown in **Figure 2** and **Table 1**. (**a-b**) Phase and amplitude distribution of the reconstructed object function without aberration correction. (**c-d**) Reconstructed object function with the aberration coefficient determined with a 5° error. (**e-f**) Reconstructed object function with the aberration coefficient determined with a 2.5° error. (**g-h**) Reconstructed object function with the aberration coefficient determined without angular error. (**i**) The phase shift in the aperture of the probe forming lens according to the aberration coefficient listed in **Table 2**. (**j-l**) The determined phase shift using SSB method in the aperture of the probe forming lens when the rotation angle error is 0°, 2.5°, and 5°, respectively. A good match between the (**i**) and (**j**) is observed, and the discrepancy becomes dramatic as the increase of the rotation angle error. Color bars of (**i-l**) represent phase shift in the unit of radian.

S10 ePIE reconstruction of an experimental dataset.

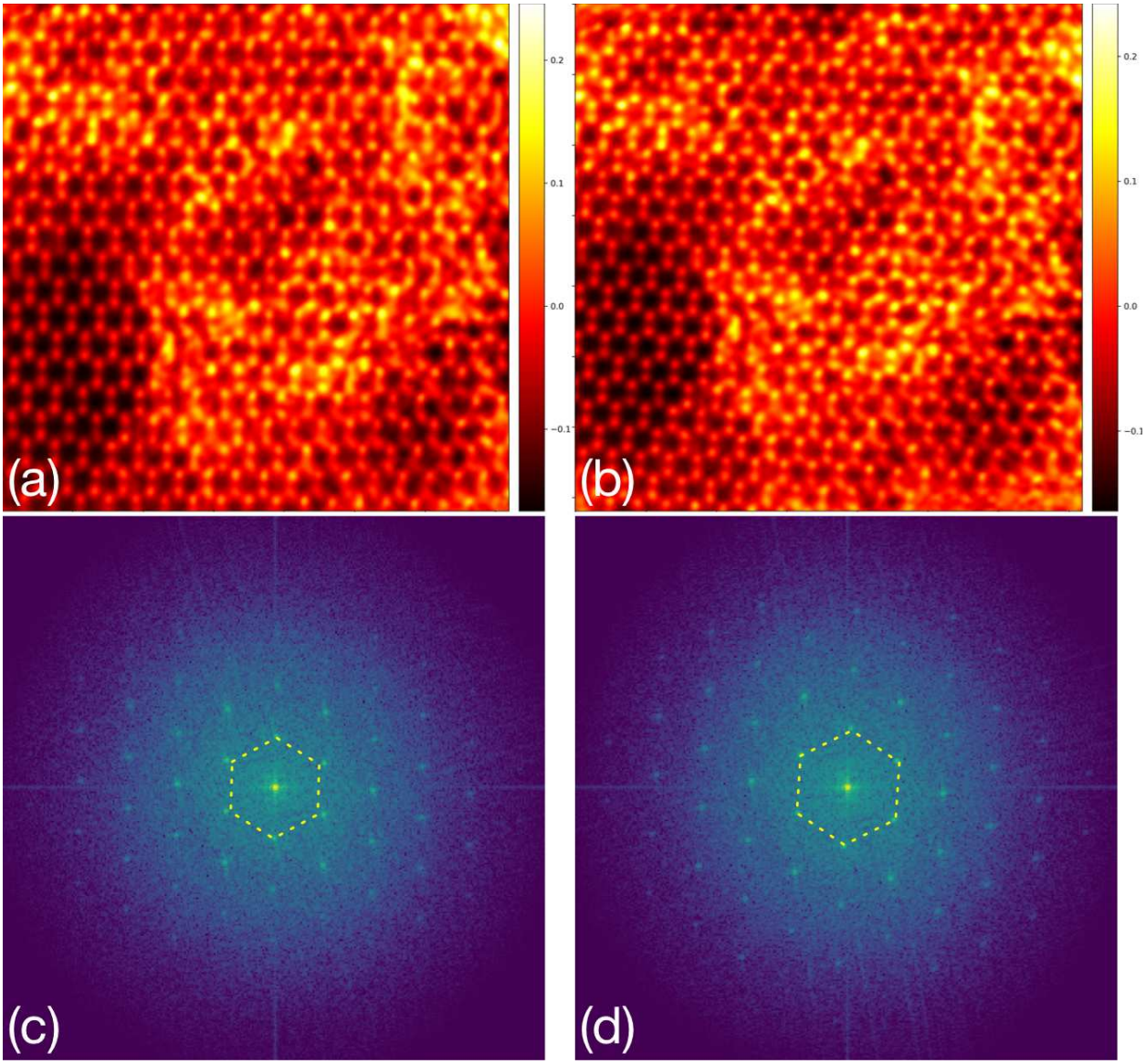

Figure S7. The phase-angle distribution and power spectrum of retrieved object using iterative ePIE reconstruction, the experimental 4D-STEM dataset shown in **Figure 6** is used. (**a-b**) The reconstructed object phase with the scanning positions initialized with the *J-matrix* method and *hybrid* method, respectively. (**c-d**) The corresponding power spectrums of computed objects with the *J-matrix* and *hybrid* calibration method, respectively. A more obvious lattice distortion in (**a**) compared to (**b**) due to uncorrected uniform scan distortions can be visualized with the help of a

dash hexagon reference overlaid on the power spectra. Color bars represent the phase shift in the unit of radian.

In the ePIE reconstruction of the experimental dataset in **Figure 6**, the position correction is enabled for both cases after the 30th iteration. An obvious elongation of the lattice is still observed in **Figure S7**(**a**) and the uniform deformation of the scanning positions is not eliminated during position correction after 500 iterations. This experimental result well matches our simulations in **Figure 8**. In comparison, the honeycomb-structured lattice of MoS_2 is recovered in **Figure S7** (**b**) when our *hybrid method* is adopted. More evidences are provided by the Bragg peaks corrected using a ortho-hexagon in the power spectrum of the reconstructed object (**Figure S7** (**d**)). In comparison, the power spectrum of the object with *J-matrix* method does not only show a degradation of resolution, especially along the vertical directions, but the {1100} Bragg peaks deviate from the hexagonal rings plotted using dotted yellow lines in **Figure S7** (**c**).

S11 Experimental 4D-STEM dataset of MoS_2.

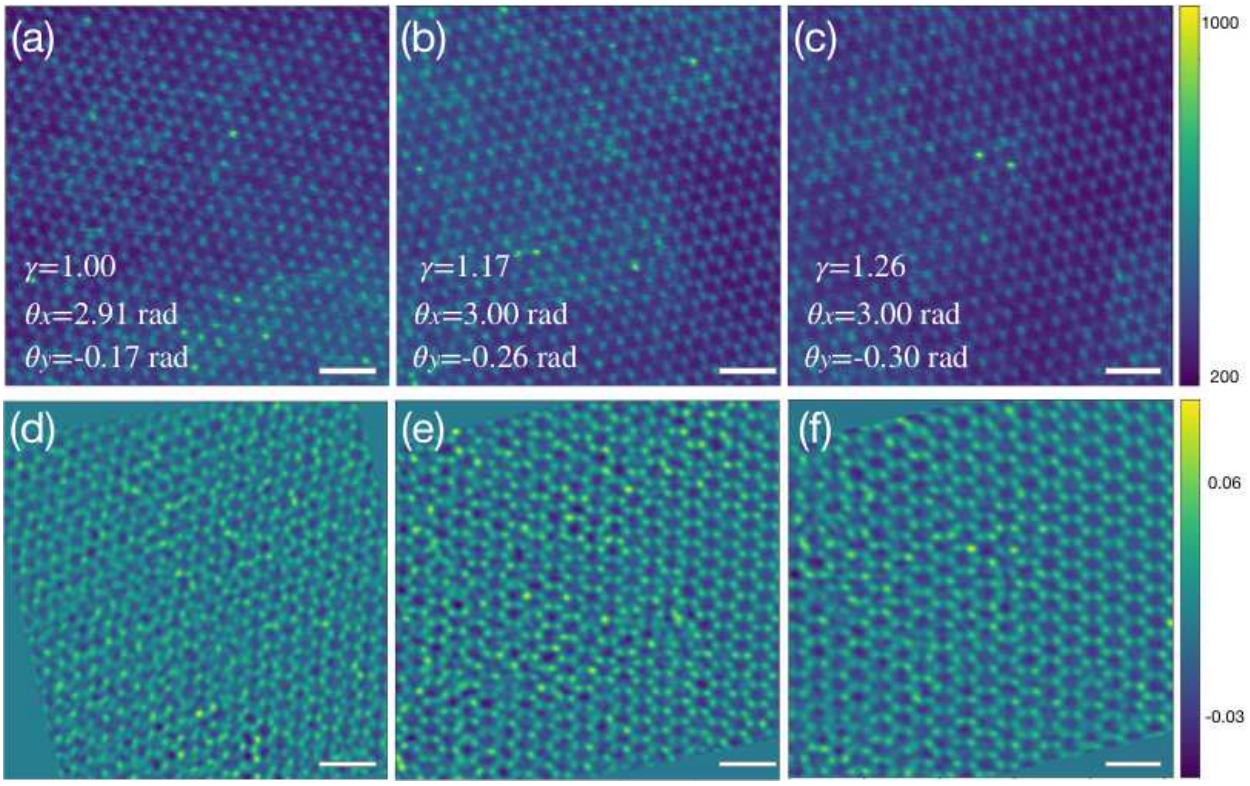

Figure S8. (**a**-**c**) Corresponding ADF-STEM images of three 4D-STEM datasets captured within the same time slot without change of samples. The sample is monolayer MoS2, and the model of the electron microscope is JEOL ARM200CF operating at 80 kV. The (**b**) and (**c**) suffer from more obvious scanning distortions compared to the (**a**) as indicated by the elongation of MoS2 hexagons along the vertical direction. (**d**-**f**). Reconstructed phase angles of (**a**-**c**). In (**d**-**f**), the scanning distortion is considered during the determination of shifted disk positions, and further compensated by applying an affine transformation to the 2D phase distribution as shown by the obvious outlines. The affine transformation successfully compensates for the uniform scanning distortion as indicated by the regular hexagons. Both local scan distortions and local strains due to defects remain in the image. Color bars in (**a**-**c**) represent the number of electrons. Color bars in (**d**-**f**) represent the phase shift in the unit of radian.

S12 Simulated 4D-STEM datasets of thick specimens.

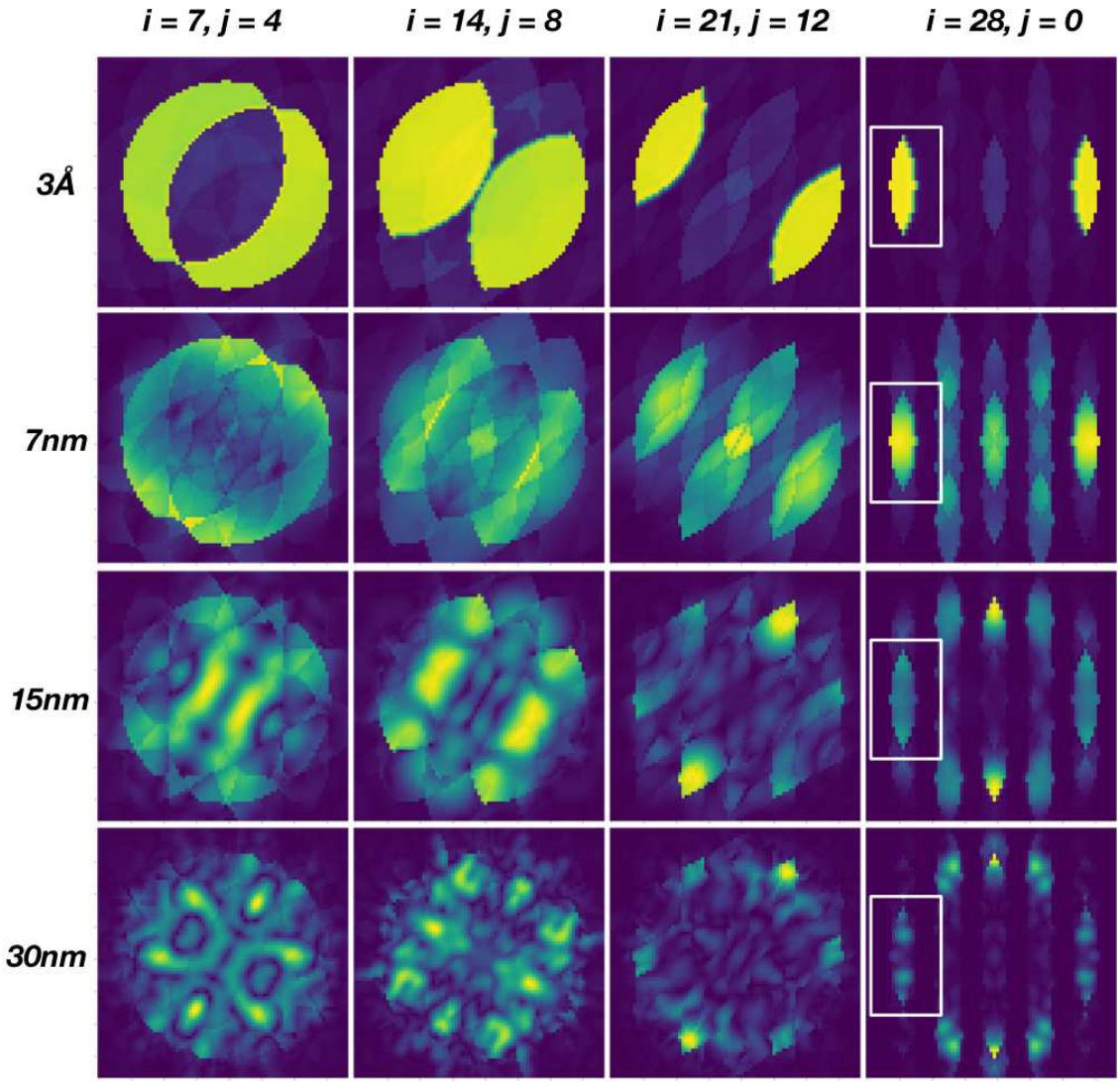

Figure S9. Simulated slices at different probe frequencies of 4D-STEM datasets of AA stacked MoS2 samples with sample thickness ranges from 3Å to 30 nm. The indexes of the probe frequencies, increasing from left to right, are (7, 4), (14, 8), (21, 12), (28, 0) respectively. The outline of the double-overlapped regions is the most obvious in the G-set slices of MoS_2 monolayer. As the sample thickness increase, the outlines of these regions are interrupted by the multiple scattering. The aperture in the averaged CBED patterns of the 30 nm MoS_2 specimen shown in **Figure S1** also has an interrupted outline. Compared to the G-set slices indexed (7, 4), (14, 8), (21, 12), the double-overlapped regions marked by the white rectangles in (28, 0) G-set slice have clear outlines.

S13 Performance of the hybrid method at the cases of low electron doses.

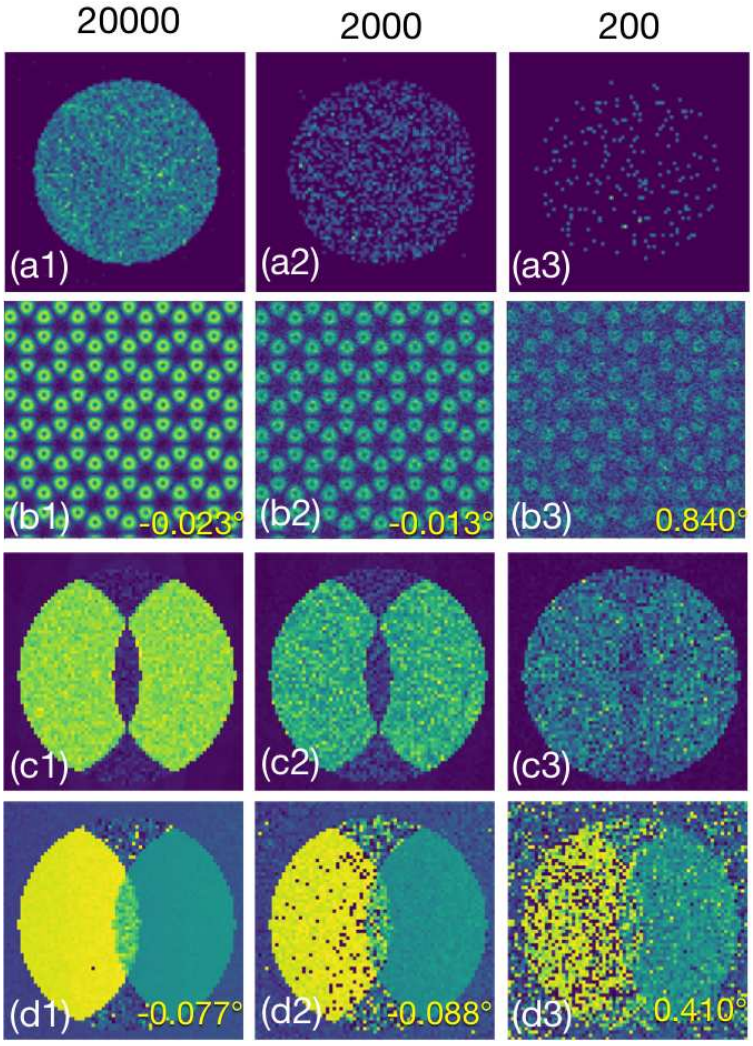

Figure S10. The low-dose performance of the *J-matrix* and the *Fourier method* involved in the hybrid method was evaluated using a similar on three simulated 4D-STEM datasets with electron doses of 6.6×10^5, 6.6×10^4, 6.6×10^3 e/Å^2. These datasets are generated based on the simulated dataset shown in **Figure 2** (**I**) with128×128 scanning positions, assuming 0° rotation angles between the scan-camera coordinates. Only random Poisson noise has been considered in the generation of low-dose datasets. (**a1**-**a3**) Representative diffraction patterns are taken from these three 4D-STEM datasets, the number of electrons for these diffraction patterns are roughly 20000, 2000, and 200, respectively. (**b1**- **b3**) The computed amplitude of the electric fields using these datasets, the contrast of the electric field degrades as the dose decreases. The determined uniform rotation angle using the J-matrix method are -0.023°, -0.013°, and 0.840°, respectively.

(**c1**-**c3**). The amplitude distribution of the G-set slice is indexed (0, 14) in different cases. (**d1**-d3). The phase distribution of the G-set slice indexed (0, 14) at different doses. It becomes increasingly difficult to distinguish the outlines of the double-overlapped regions in G-set slices in both amplitude and phase pictures as the dose decreases. Using the phase images of the G-set slices, the rotation angle by fitting the diffracted disks are -0.077, 0.088, and 0.410, respectively. The accelerating voltage used in the simulation was 80kV and more details can be found in **Supporting Materials S2.**

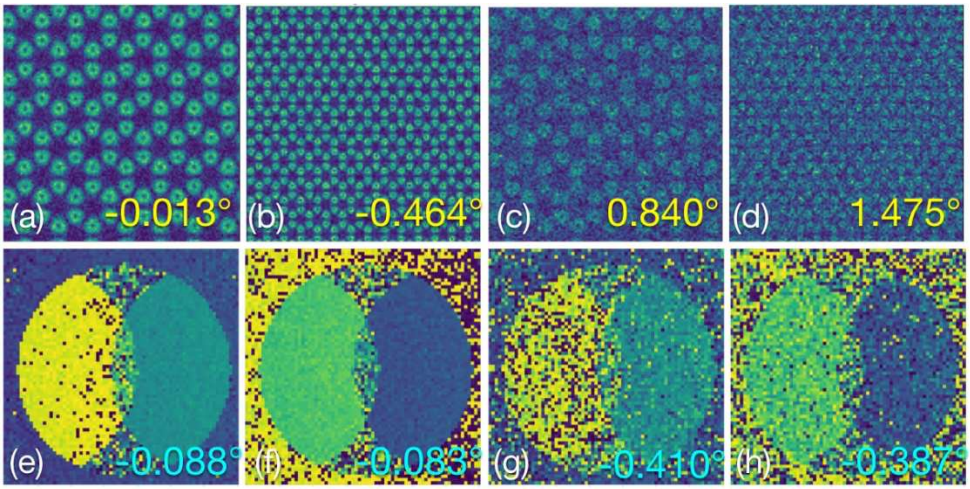

Figure S11. Additional discussion about the dose effect on the J-matrix method and the Fourier method. (**a**-**d**) The computed amplitude of the electric fields and the corresponding calibrated uniform rotation angles using the J-matrix method, which are -0.013°, -0.464°, 0.840° and 1.475°, respectively (**e**-**h**) The phase distribution of the G-set slice indexed (0, 28) and the corresponding calibrated uniform rotation angles using the Fourier method, which are -0.088°, -0.083°, -0.410° and -0.387°. (**a**) (**e**), (**b**) (f), (**c**) (g) and (**d**) (**h**) are obtained from the same simulated datasets. (**b**) and (**d**) are related to (a) and (c) in the way that the field of view was englarged by 4 times, but the total number of electrons in the dataset remain unchanged: (**a**,**e**) - 6.6×10^4 e/Å^2;(**b**,**f**) - 1.65×10^4 e/Å^2 ; (**c**,**g**) - 6.6×10^3 e/Å^2; (**d**,**h**) - 1.65×10^3 e/Å^2 . (**a**) and (**c**) are the same data as in **Figure S10** (**b2**) and (**b3**), respectively. The accuracy of the Fourier method remains largely unchanged as long as the total number of electrons in the dataset were kept the same. This is not the case for the J-matrix method. The accelerating voltage used in the simulation was 80kV, with 128 by 128 probe positions and 0° angle between the scan-camera coordinates. More details can be found in **Supporting Materials S2.**

S14 Testing the hybrid method on simulated amorphous carbon.

The *hybrid* method was tested using a simulated 4D-STEM dataset of the amorphous carbon, which not only is more complicated than crystalline MoS_2, but also has small projected interatomic spacings within. As shown in **Figure S12** below, we found that both the *J-matrix* method and the *Fourier* methods (two sub-routines for the *hybrid* method) behaves exactly the same as in the case of MoS_2 sample: (i) the *J-matrix* method is still able to find the correct rotation angle using the target function discussed in **Figure 1**; (ii) the disks are clearly visible in the G-slices and the shift vector **Q** and the angle α defined in **Figure 3** can be easily determined. Hence the *hybrid* method will be able to function properly in the case of the amorphous carbon specimen, which is structurally much more complicated than single layer MoS_2 specimen. We can safely say that material is not the limiting factor as long as the weak phase object approximation holds.

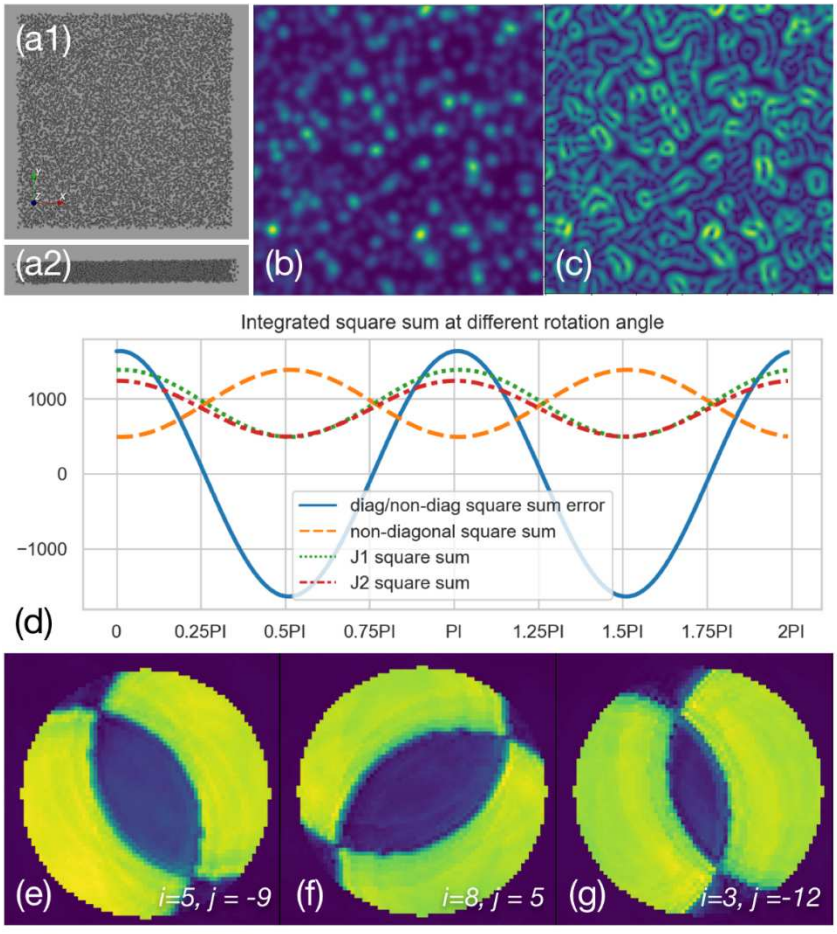

Figure S12. Testing the hybrid method using a simulated 4D-STEM data from the amorphous carbon. (**a1** –**a2**). The top-view and the cross-section view of a thin amorphous carbon model. The

thickness of this amorphous carbon sample is set to 2nm, and the minimum distances between the carbon atom is set to 1.4 Å. In the 4D-STEM simulation, the aperture of the probe-forming lens is set to 30 mrad, and the accelerating voltage is set to 80 kV. The scanning interval and defocus are 0.35 Å and 0 nm, respectively. The 4D-STEM dataset consists of 128*128 diffraction patterns, and each diffraction pattern have 256*256 pixels. The angular ranges of the diffraction pattern along horizontal and vertical directions are both 240 mrad. (**b**). The computed ADF-STEM image from the 4D-STEM dataset of the thin amorphous carbon model. (**c**). The computed modulus of the electric filed from the 4D-STEM dataset of the thin amorphous carbon model. (**d**). The integrated squared Jmatrix terms at different rotations angles. The computed relationship between the Jmatrix and the rotation angle is the same as the one give in **Figure 1**(**f**). **(e–f).** The intensity distribution of the G-set slice of different (i,j) coordinates. The disks are clearly visible so that the vector **Q** and the angle α defined in **Figure 3** can be determined.

S15 Estimation of computation time/requirement for a typical 4D-STEM dataset between the case of using the hybrid method and the case of using the J-matrix method alone.

For a typical 4D-STEM dataset like the experimental dataset given in **Figure 6** consisting of 256*256 diffraction patterns with 256*256 pixels as an example, the time cost using the J-matrix code is around 44.5 seconds including the time cost of generating the STEM and electric field images for data visualization, the cost of the computer RAM is around 4.0GB since the experimental dataset is stored in 8 bit. When applying the Fourier method, the time and RAM cost dramatically increase to 122.3 seconds and 32GB since the Fourier transform of the 4D-STEM dataset is needed.

Reference

Hachtel, J. A., Idrobo, J. C. & Chi, M. (2018). Sub-Ångstrom electric field measurements on a universal detector in a scanning transmission electron microscope. *Advanced structural and chemical imaging* **4**, 10.

Maiden, A. M. & Rodenburg, J. M. (2009). An improved ptychographical phase retrieval algorithm for diffractive imaging. *Ultramicroscopy* **109**, 1256–1262.